

INFORMATION TO USERS

This manuscript has been reproduced from the microfilm master. UMI films the text directly from the original or copy submitted. Thus, some thesis and dissertation copies are in typewriter face, while others may be from any type of computer printer.

The quality of this reproduction is dependent upon the quality of the copy submitted. Broken or indistinct print, colored or poor quality illustrations and photographs, print bleedthrough, substandard margins, and improper alignment can adversely affect reproduction.

In the unlikely event that the author did not send UMI a complete manuscript and there are missing pages, these will be noted. Also, if unauthorized copyright material had to be removed, a note will indicate the deletion.

Oversize materials (e.g., maps, drawings, charts) are reproduced by sectioning the original, beginning at the upper left-hand corner and continuing from left to right in equal sections with small overlaps. Each original is also photographed in one exposure and is included in reduced form at the back of the book.

Photographs included in the original manuscript have been reproduced xerographically in this copy. Higher quality 6" x 9" black and white photographic prints are available for any photographs or illustrations appearing in this copy for an additional charge. Contact UMI directly to order.

U·M·I

University Microfilms International
A Bell & Howell Information Company
300 North Zeeb Road, Ann Arbor, MI 48106-1346 USA
313/761-4700 800/521-0600

Order Number 1349135

**Estimating surface precipitation over Mexico by calibrating
satellite infrared imagery and airborne radar**

Schmitz, Jeffrey Todd, M.S.

The University of Arizona, 1992

U·M·I
300 N. Zeeb Rd.
Ann Arbor, MI 48106

ESTIMATING SURFACE PRECIPITATION OVER MEXICO BY CALIBRATING
SATELLITE INFRARED IMAGERY AND AIRBORNE RADAR

by

Jeffrey Todd Schmitz

A Thesis Submitted to the Faculty of the

DEPARTMENT OF ATMOSPHERIC SCIENCE

In Partial Fulfillment of the Requirements
For the Degree of

MASTER OF SCIENCE

In the Graduate College

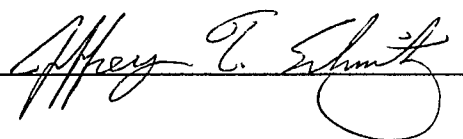
THE UNIVERSITY OF ARIZONA

1 9 9 2

STATEMENT BY AUTHOR

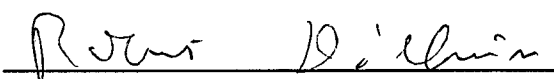
This thesis has been submitted in partial fulfillment of requirements for an advanced degree at The University of Arizona and is deposited in the University Library to be made available to borrowers under the rules of the library.

Brief quotations from this thesis are allowable without special permission, provided that accurate acknowledgment of source is made. Requests for permission for extended quotation from or reproduction of this manuscript in whole or in part may be granted by the head of the major department of the Dean of the Graduate College when in his or her judgment the proposed use of the material is in the interests of scholarship. In all other instances, however, permission must be obtained from the author.

SIGNED: 

APPROVAL BY THESIS DIRECTOR

This thesis has been approved on the date shown below:



R. E. Dickinson

Professor of Atmospheric Science

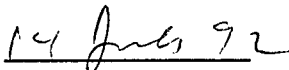

Date

Table of Contents

| | |
|---|----|
| List of Illustrations | 4 |
| List of Tables | 5 |
| ABSTRACT | 6 |
| 1. Introduction | 7 |
| 2. Data | 14 |
| 3. Method of Analysis | 24 |
| 3.1 Correlation and Regression Analysis | 26 |
| 3.2 Regression Line Combination | 33 |
| 3.3 Daily Rainfall Estimation | 35 |
| 4. Results of Correlation and Regression Analysis | 46 |
| 5. Results of Regression Line Combination | 67 |
| 6. Results of Daily Rainfall Estimation | 75 |
| 7. Summary and Conclusions | 86 |
| References | 92 |

List of Illustrations

| | |
|--|----|
| Figure 1. Internal Reflectivity and Satellite Infrared Fields | 19 |
| Figure 2. GOES Infrared Images | 25 |
| Figure 3. Scatter Diagrams | 59 |
| Figure 4. Estimated Internal Reflectivity Fields | 66 |
| Figure 5. Regression Lines | 71 |
| Figure 6. Scatter Diagrams for ATI/HART Slope Parameter Estimation | 81 |

List of Tables

| | |
|---|----|
| Table 1. Cases Studied and Sample Identifiers | 29 |
| Table 2. Correlation and Regression Results | 49 |
| Table 3. Regression Equations | 50 |
| Table 4. Rainfall Estimation Results | 82 |

ABSTRACT

An algorithm for estimating daily surface rain volumes from hourly GOES infrared images has been developed using data obtained during the Southwest Area Monsoon Project (SWAMP). Daily surface rain volumes will be estimated using derived positive linear relationships between digital infrared counts and cloud radar reflectivities. These relations provide estimates of radar reflectivities corresponding to hourly infrared images, which in turn, using an assumed reflectivity-rainrate (ZR) relation ($Z = 55R^{1.6}$), will be used to generate hourly precipitation fields from which daily rain volumes are computed. The linear relations employed are determined through a regression analysis on digital IR counts of GOES imagery and airborne internal radar reflectivity samples. This study also explores the existence of an average linear relation between infrared pixel values and radar reflectivities.

1. Introduction

Recent studies of the southwestern United States and Mexico have revealed that weather in this region is characterized by two distinct climatological regimes. From October through May the mean middle and upper level tropospheric flow is typically from the west, with precipitation resulting primarily from cyclonic storm systems originating over the Pacific ocean and migrating eastward. During the summer season (June-Sept.), however, a pronounced 'monsoonal' reversal of the mean winds occurs such that easterly or southeasterly winds now describe the 700 mb to 500 mb streamlines. As a result, the generally dry stable air mass of fall and winter is replaced by a moist unstable one. (Maddox, Douglas, and Howard, 1991; Douglas, Maddox, Howard, and Reyes, 1992; Smith and Gall, 1989).

Concurrently, the dominant precipitation mechanism undergoes a noticeable transformation. Rainfall no longer comes primarily in the form of large scale synoptic disturbances, but instead takes on a distinctly convective nature. Aided by the moisture flux accompanying the seasonal wind reversal, the summertime period is characterized by a much higher frequency of convective storms as determined by Maddox, Howard, Douglas, and Negri (1992) in their analysis of the frequency of occurrence of cloud top temperatures less than -36° C.

Although mesoscale systems are much more localized than

synoptic ones, the higher frequency of convective storms produces a notable increase in precipitation amounts. In fact, virtually all Mexican stations receive more than 60% of their annual rainfall between July and September, while the southwestern United States receives upwards of 40%. Further analysis reveals that the largest changes in rainfall amounts occur between June and July, where differences in monthly totals exceed 200 mm for some Mexican stations (Douglas, Maddox, Howard, and Reyes, 1992). Even though both Mexico and the SW United States have precipitation maximums during the monsoon period, Mexican rainfall is substantially greater, with highest totals occurring on the western slopes of the Sierra Madre Occidental. It appears then, that the SW United States is merely on the fringe of a more pronounced Mexican monsoon (Douglas, Maddox, Howard, and Reyes, 1992).

Precipitation events of the southwest area monsoon are associated with easterly waves, depressions along the monsoon (or moist air mass) boundary, weakening tropical cyclones, and mesoscale convective systems (Smith and Gall, 1989). Since the three synoptic disturbances generally lead to formation of the mesoscale convective systems (MCS), Maddox, Douglas, and Howard (1991) have further categorized these as one of three types: individual and short-lived multicell thunderstorms; meso-beta scale convective systems; and meso-alpha scale convective systems.

When the moist monsoonal air mass is in place, individual and short-lived multicell thunderstorms occur almost daily, as orographic lifting provides an efficient means for releasing the present convective instability(Maddox, Douglas, and Howard, 1991). Typically, these systems consist of individual convective elements which produce heavy rain showers of limited spatial and temporal extent. Although extensive anvil cloudiness has been observed, these storms generally do not develop the stratiform precipitation common to more organized convective systems(Maddox, Douglas, and Howard, 1991).

Reflectivity studies of individual thunderstorms reveal that mature convective regions exhibit high reflectivities(DBZ) extending nearly as high as the corresponding cloud top(Saunders and Ronne, 1962). Since multicell storms can be thought of as a "cluster of short lived single cells"(Weisman and Klemp, 1986), it is apparent that multicell storms would display a reflectivity pattern similar to the distribution of individual convective elements. Studies of multicell systems indicate a progression of developing, mature, and dissipating convective cells spanning the length of the storm from front to rear. Analogous to this pattern is a series of varying echo intensities which increase in magnitude as convective cells mature, and decrease as these cells dissipate(Weisman and Klemp, 1986).

Meso-beta scale convective systems are defined as having length scales of 25 km to 250 km and lifetimes of less than six hours (Maddox, 1980). These systems are considerably more organized than the multicell or individual thunderstorms discussed above. Proliferation of beta-scale storms typically occurs through discrete propagation, as cold outflows from mesoscale downdrafts initiate the development of new convective cells on the leading edge of the existing system (Maddox, Douglas, and Howard, 1991; Smith and Gall, 1989). Reflectivity studies indicate that some of these systems have intense convective elements and extensive anvil precipitation, while other systems show only disorganized convection and little if any stratiform precipitation (Schuur, 1991; Maddox, Douglas, and Howard, 1991; Bartels, 1991). As a result, meso-beta systems can display either random or well organized radar returns. The latter consists of cellular, moderate to high intensity echoes coupled to a less intense and more uniform, or stratiform, reflectivity region (Schuur, 1991; Leary and Houze, 1978; Smull and Houze, 1985 and 1987)

The largest MCS observed during the monsoon period is the meso-alpha scale convective system. These storms typically have length scales of 250 km to 2500 km and durations of greater than six hours (Maddox, 1980). Better known as tropical squall lines and tropical mesoscale convective complexes (MCC's), these systems exhibit characteristics

similar to middle latitude squall lines and middle latitude MCS's, respectively(Howard and Maddox, 1988; Maddox, Douglas, and Howard, 1991; Smull, and Houze, 1987).

Thus tropical squall lines generally consist of a rapidly moving line of convective precipitation followed by stratiform cloud and light rain(Smull and Houze, 1987; Smith and Gall, 1989). Consisting of a series of developing, mature, and dissipating cells resulting from discrete propagation, the cumulonimbus line exhibits a reflectivity field similar to the multicell thunderstorm. The stratiform region, on the other hand, consists of a more uniform reflectivity field superimposed around a middle-level bright band corresponding to the melting layer(Smull and Houze, 1987; Gamache and Houze, 1982).

Unlike linear meso-alpha systems, tropical MCC's are circular, or elliptical, with convective elements lying on the perimeter. Due to the mesohigh which develops in the center of this storm, cold outflow from internal stratiform precipitation leaves the system in a nearly circular fashion and serves as a lifting mechanism for incoming, unstable environmental air(Maddox, 1980). Thus, convective elements can be distributed randomly about the perimeter of the cloud shield, but more often develop ahead of the system in the direction of propagation. As a result, radar echoes display a circular or elliptical shape similar to the cold cloud shield, where high reflectivities appear almost col-

located with coldest cloud tops(Maddox, 1980; Leary and Rappaport, 1983).

Of the three MCS's discussed above, satellite imagery has revealed that individual storms and beta scale complexes are the dominant precipitation mechanisms of the Southwest Area Monsoon(Maddox, Douglas, and Howard, 1991). As key components of monsoon rainfall in the southwestern United States and Mexico, these storms play a vital role in the local hydrological cycle. However, due to the complex orography of this region and inadequate meteorological observations, quantitative and temporal measurements of surface precipitation are difficult(Maddox, Douglas, and Howard, 1991). To further our understanding in this area, the National Severe Storms Laboratory(NSSL), in conjunction with several other institutions(see SWAMP 1991), conducted the Southwest Area Monsoon Project(SWAMP) during the summer of 1990. This project yielded information pertaining to the internal radar reflectivity structure, evolution, and precipitation of southwest area MCS's(SWAMP, 1991).

Using satellite infrared, aircraft radar reflectivity, and surface rainfall data from the SWAMP database, this paper focuses on the estimation of surface precipitation from space. In consideration of the fact that, 1) high cloud tops correspond to low cloud top temperatures, or high digital infrared counts, 2) radar echoes of mature convective cells extend nearly to the top of the cloud, and

3) horizontally homogeneous stratiform clouds tend to display horizontally uniform reflectivity fields, it is reasonable to assume a positive linear relationship between satellite derived cloud top temperatures(or digital IR counts) and internal radar reflectivities. Also, since radar reflectivities can be related to surface rainfall rates(Battan, 1973; Bohren and Huffman, 1983; Atlas, 1990), it is hypothesized that surface rainfall can be estimated from satellite IR images using a linear relation between digital IR counts and internal reflectivities in conjunction with a regionally tuned reflectivity-rain rate(ZR) relationship.

Therefore, it is the purpose of this paper to estimate daily surface rainfall from hourly GOES infrared images, through the estimation of internal radar reflectivity(DBZ) from these images, followed by the application of a regional reflectivity-rainrate(ZR) relation to the resulting DBZ values. This will be accomplished by first correlating internal radar reflectivities with digital infrared(IR) counts of satellite images. Following this, a linear regression between DBZ values and IR counts will be performed. Assuming that a positive relationship between IR and DBZ values are found, the regression analysis will produce predictor equations from which internal radar reflectivities can be estimated from the digital infrared counts of GOES images. Once the reflectivity field corre-

sponding to a given infrared image has been produced, surface rainfall will be estimated on a grid point basis by determining the surface rainfall rate corresponding to the estimated DBZ values using $Z = 55R^{1.6}$, where Z is radar reflectivity and R is the hourly rainfall rate. Daily volumetric rainfall totals will then be determined using a simple grid point summation and two area-time integral approaches.

An additional topic of this paper focuses on the uniqueness of the linear relationship derived for the internal reflectivity estimation. Are the relationships independent of the convective or stratiform nature of the cloud observed? Or do they depend on factors such as cloud type, type of storm, and climatology of the day?

2. Data

During SWAMP, internal reflectivity data for several MCS's were obtained using the National Oceanic and Atmospheric Administrations (NOAA) P-3 Orion aircraft. Reflectivity measurements were taken by the P-3's vertically scanning, 3.2 cm tail radar using a Forward-Aft Scanning Technique (FAST) as described by Schuur (1991). For the purpose of this study reflectivity data for three MCS's observed during SWAMP have been chosen.

Case one, a west coast meso-alpha scale convective complex observed during the mature to dissipating stages of

its lifecycle, occurred on July 12, 1990 and was positioned at approximately 25N and -107.9W. This system existed for almost eleven hours(2200 - 0800 UTC) and displayed considerable organization. In-flight observations describe a convective line with cells of 60 DBZ and 18 Km heights, coupled to a trailing stratiform precipitation region. GOES imagery revealed an extensive anvil with cloud top temperatures as low as -72°C . The 0000 UTC sounding over Mazatlan(23.2N, -106.42W) indicated that this system developed in an extremely moist and unstable air mass. Surface relative humidity was reported as 71% which, for a surface temperature of $\sim 31^{\circ}\text{C}$, required a dew point temperature(T_d) of 25.6°C . Furthermore, precipitable water(PW) for a column of atmosphere(of 1 cm^2 cross sectional area) extending from the surface to the top of the atmosphere was 5.30 cm. The Lifting Condensation Level(LCL) at this time was situated at 925 mb and accompanied by a Level of Free Convection(LFC) at 893 mb. This shows that minimal lifting was required to release the present instabilities. In fact, the surface temperature required for convective clouds to develop by pure thermal buoyancy alone was 30.6°C corresponding to a Convective Condensation Level(CCL) of 944 mb. Lower than the current surface temperature, this convective temperature was coupled with moist, low level 'upslope' westerly winds and topped off by drier easterlies aloft(at 850, 700, and 500mb), indicating the environment was ripe

for convective outbreaks. Further evidence of this instability was a Lifted Index(LI) of -6.3. An inverted trough associated with an easterly wave in the low and middle level flow appeared to aid the development of storms on this day.

The meso-beta system selected for case two occurred over Sonora(30.7N,-110.6W) on July 17, 1990. Unlike the system of case one, this MCS had a duration of about four hours(2000-2300 UTC) and consisted of randomly organized convective cells with reflectivities of 40-50 DBZ and cloud heights of 16 Km. GOES imagery revealed that this system failed to develop an extensive anvil cloud shield and thus, a trailing region of stratiform rainfall. Therefore, this storm was considered of the multicell variety. Lowest cloud top temperature derived for this system was -63° C. Synoptic observations of the day reveal a distinct dry slot over central Arizona and northern Mexico. Smith and Gall(1989) describe this condition as favorable for the development of significant monsoonal events. Local conditions indicated by the 1200 UTC Empalme sounding describe a moist unstable air mass($T_d = 25^{\circ}$ C, PW = 4.78cm) as in case 1, but on this day the probability of convective outbreaks were not as great, as indicated by a smaller Lifted Index of -3.3 and larger convective temperature(34.7° C). Although the LCL(990mb) was much lower than that of case 1, both the LFC(860mb) and the CCL(893mb) were higher. Thus, more lifting was required for

convection to develop and probably resulted from low level westerlies encountering the Sierra Madre Occidental. The entire lifecycle of this storm was observed by the P-3 tail radar.

Case three consists of a MCS occurring on July 20, 1990 and previously studied by Schuur(1991). This meso-beta system was located approximately 100 km south of the Arizona-New Mexico border(29.6N,-108.9W) and was composed of a distinct line of convective cells, which later developed a stratiform precipitation region. In-flight observations noted cloud top heights of 18 Km and internal reflectivities as high as 60 DBZ. Satellite derived cloud top temperatures were as low as -76°C . This system lasted approximately six hours and formed in an environment similar to case two(PW = 5.63cm, LI = -3.2, LCL = 905mb, LFC = 897mb, and CCL = 887mb), but with low level southerlies or southeasterlies instead of westerlies. With the upslope forcing missing on this day, another means for releasing the instability was required. This came in the form of mid-level divergence associated with a 700 mb anticyclone located over west central Arizona.

Each of the cases described above consists of three airborne reflectivity samples collected during P-3 operations. Due to the X-band operating wavelength the maximum unambiguous radar range was limited to 76 Km(SWAMP, 1991). Thus, the complete instantaneous observation of internal radar

reflectivities for each system was impossible. Therefore, each reflectivity sample will correspond to a given region of the cloud with the sample size being dependent on the duration of the observation and the flight track of the aircraft. In this analysis, all reflectivity samples consist of sixteen horizontal 225×225 km² grids spanning the vertical depth of the scanned region. Horizontal resolution in each grid is 3 Km. Figure 1 depicts vertically averaged horizontal reflectivities for each sample. Table 1 lists each sample, time of observation, and region of storm observed.

The convective or stratiform nature of each cloud region was determined by the SWAMP in-flight observers using a technique presented in Watson, Meitin, and Cuning(1988). This method distinguishes between convective and stratiform cloud types through consideration of the areal extent, DBZ thresholds, and overall longevity of the echo patterns displayed on a radar screen. First of all, any radar echoes bounded by a contour of less than 30 DBZ whose area is less than 10^3 km² is deemed convective. Echoes with larger areal coverage are assumed to contain both stratiform and convective elements. To identify embedded convective areas, consideration is given to the cellular nature and duration of the echo patterns. Since convective clouds are felt to be areas of intense, rapidly fluctuating, high reflectivity cores, regions where echo magnitudes and distributions vary

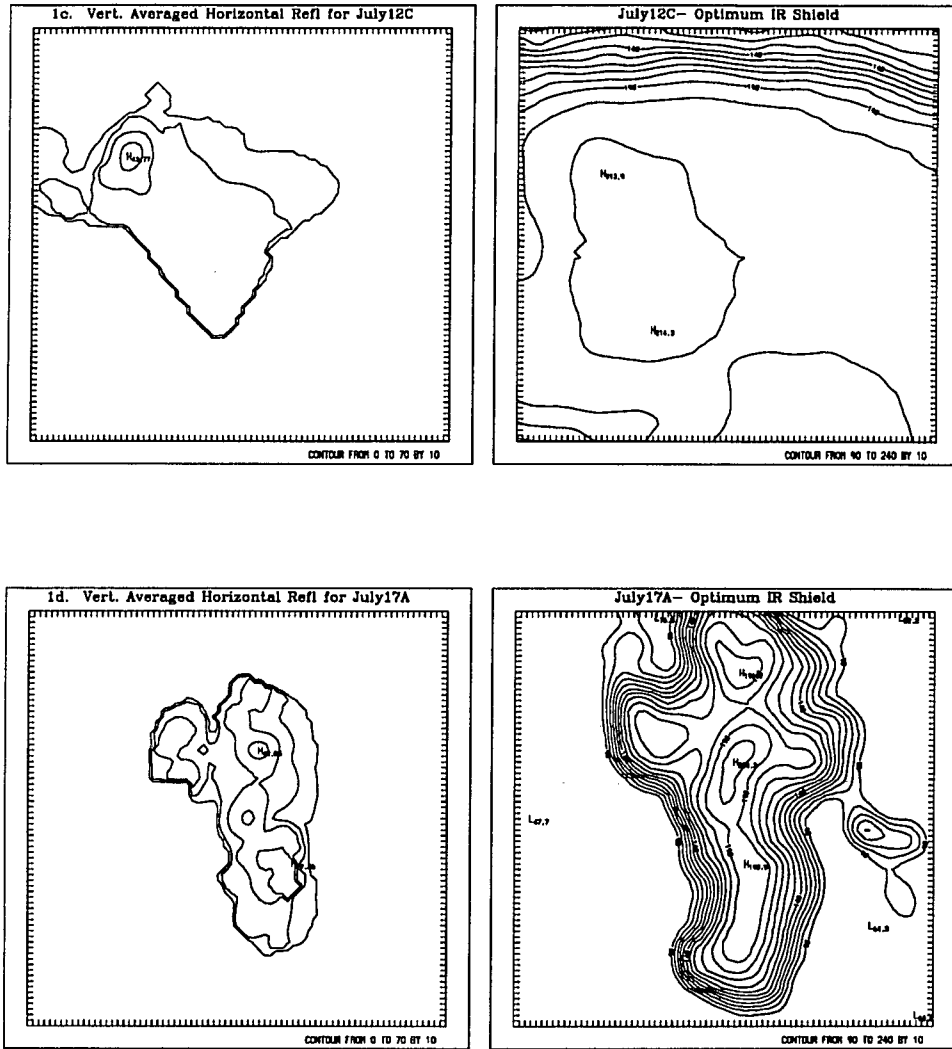


Figure 1.
Vertically averaged horizontal radar reflectivities and corresponding optimal infrared images continued.

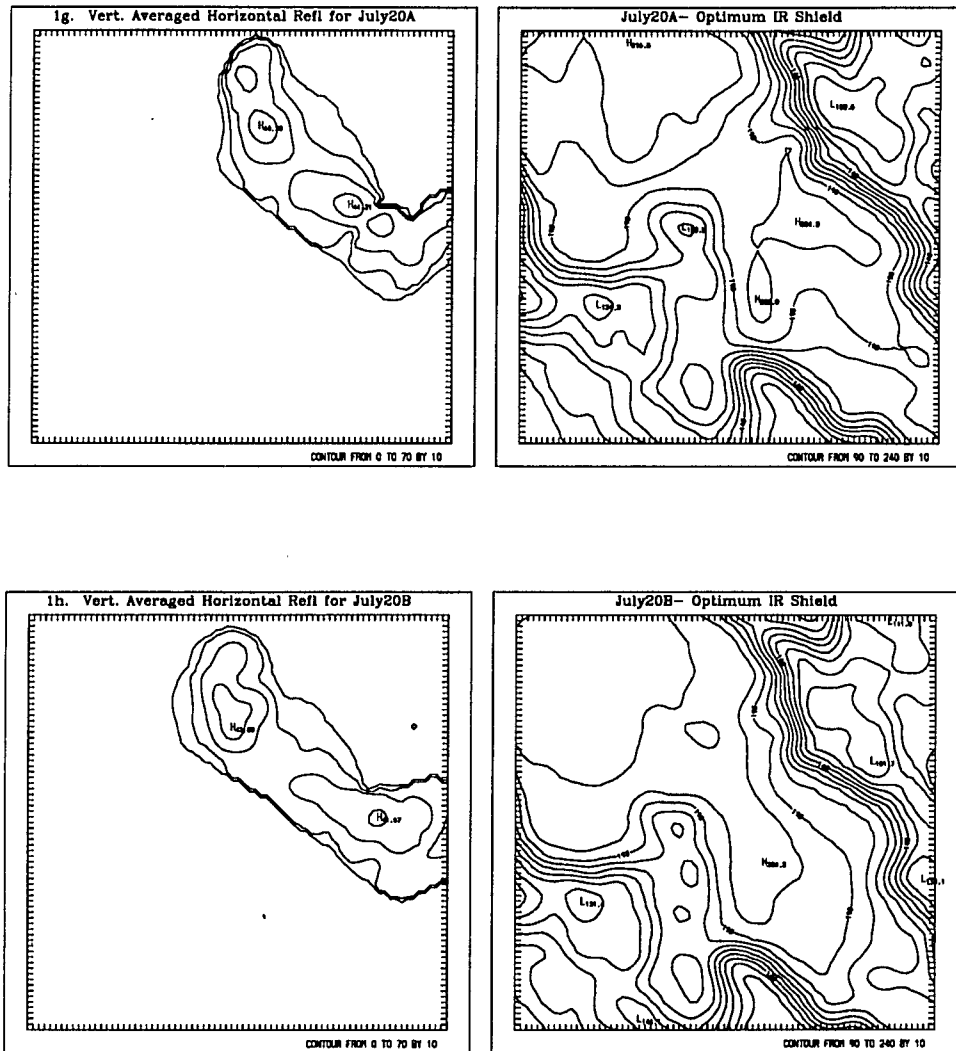


Figure 1.

Vertically averaged horizontal radar reflectivities and corresponding optimal infrared images continued.

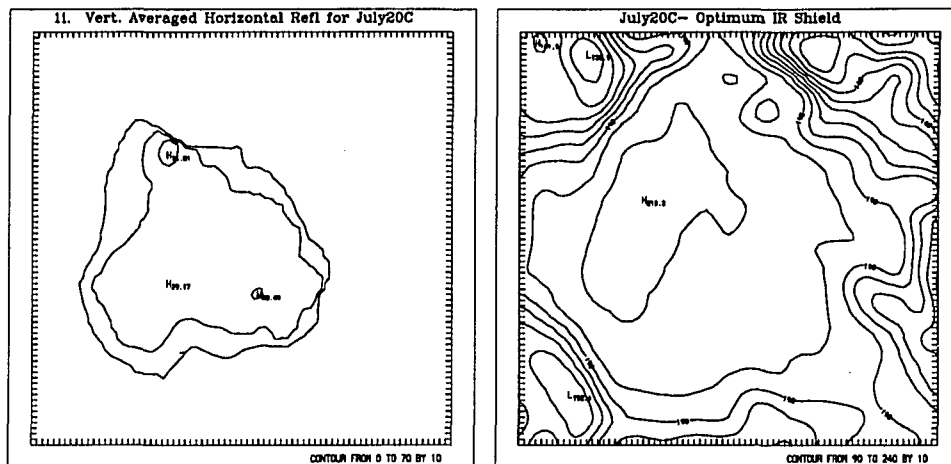


Figure 1.

Vertically averaged horizontal radar reflectivities and corresponding optimal infrared images continued.

considerably over fifteen minute time intervals are classified convective in nature. More persistent reflectivity regions are therefore classified as stratiform cloud (Watson, Meitin, and Cuning, 1988).

Along with internal reflectivity data, this analysis will employ infrared imagery provided by Global Operational Environmental Satellites (GOES). During SWAMP, GOES infrared, visible, and water vapor imagery were collected and archived at NSSL in Boulder, Colorado. Hourly infrared imagery, with approximately 8 Km horizontal resolution, was

collected on the FSL national scale, which includes the contiguous 48 states, southern Canada, and portions of Mexico above 20 degrees north latitude (SWAMP, 1991). For this study, 480x480 km² subsectors of full sector GOES images have been extracted for the purpose of isolating the individual mesoscale convective systems described earlier. Since the radar reflectivity samples described above correspond to time increments lying between the hourly GOES intervals, the hourly GOES images were linearly interpolated to correspond to the median time of the radar observation. This was felt to provide a more representative infrared sample with which to perform the correlation and regression analysis. Figure 2 presents the interpolated infrared images to be used for each of these systems.

In addition to the reflectivity and satellite data described above, SWAMP employed an extended surface rain gauge network over Sonora and along the west coast of the Sierra Madre Occidental. Daily rainfall totals are available for two hundred sites in Mexico and will be used in the estimate of daily rain volumes.

3. Method of Analysis

In order to estimate rainfall over Mexico from satellite infrared imagery, this analysis will consist of three components. The first aspect will focus on establishing positive linear relationships between the digital IR counts and

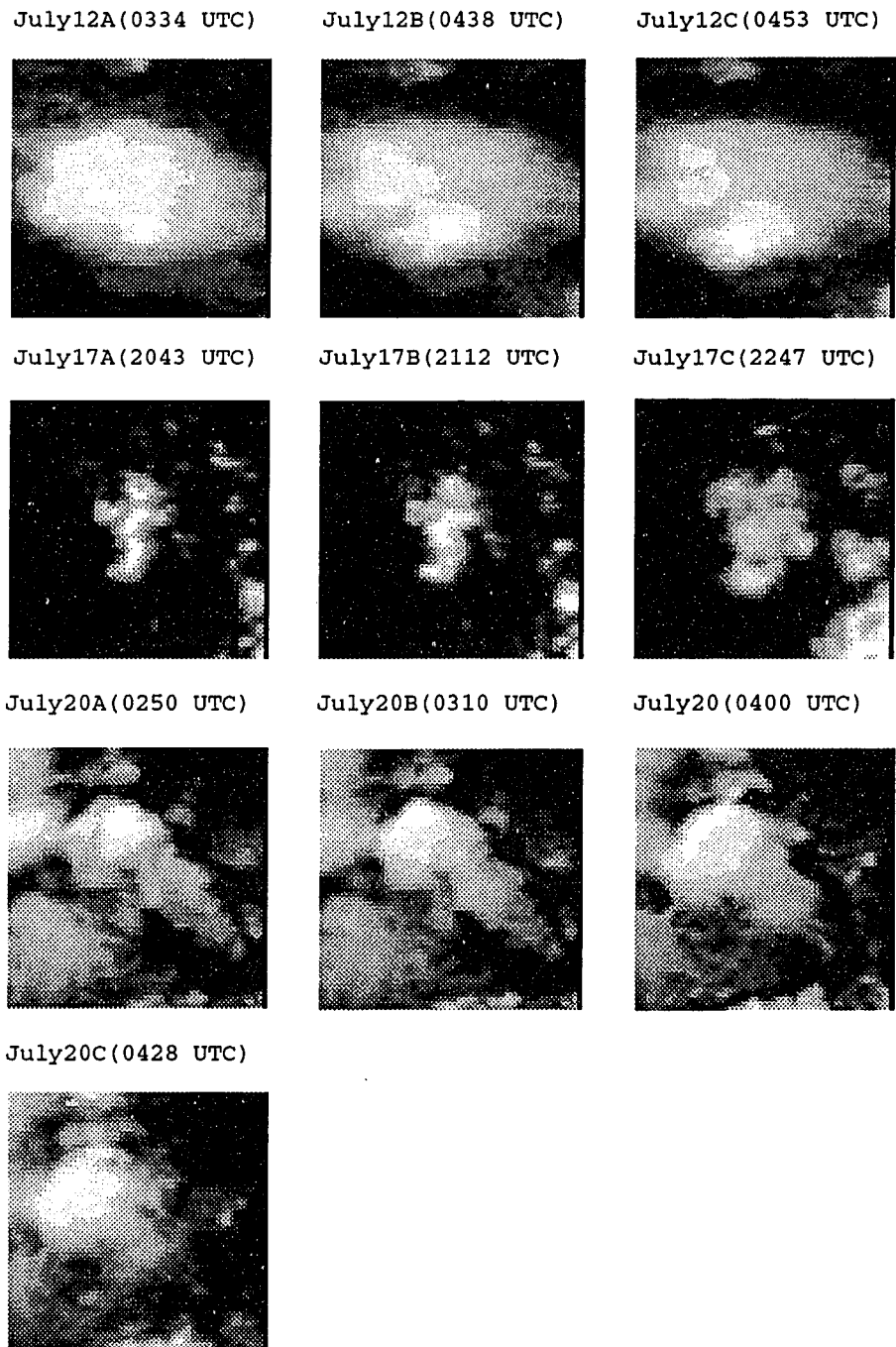
Figure 2. GOES Infrared Images

Figure 2. Infrared subsectors extracted from full sector GOES images.

internal reflectivities of the grids presented in Figure 1. This will be accomplished by performing a correlation and least squares regression analysis for each of the nine image pairs.

Assuming a positive relationship is established, the second aspect of this study will compare the nine regression equations resulting from the first phase of the analysis. Are these relationships distinct for each grid pair, or can some of them be considered the same?

Regardless of the outcome of regression line combination, the third component of the analysis will be the estimation of daily rain volumes for selected regions in Mexico. This will be accomplished using the regression equations derived previously. These will be employed to estimate internal reflectivity fields corresponding to hourly GOES infrared images. The resulting reflectivities will provide DBZ values from which surface rainfall will be estimated using a local reflectivity-rainrate relation.

In the paragraphs that follow, each phase of this study will be thoroughly discussed in the order presented above. Starting with the correlation and regression analysis, any assumptions, equations, or procedures used in each step will be considered.

3.1 Correlation and Regression Analysis

Utilizing satellite infrared and airborne reflectivity

data for the three MCS's described earlier, correlation between cloud top temperatures and reflectivity values will be analyzed through least squares linear regression. This will be accomplished by first mapping the 8 km resolution infrared images into the 3 km resolution reflectivity grid by way of a Cressman weighting scheme. In this approach, each grid point of the higher resolution grid will be assigned a value according to its distance from grid points of the satellite image to be remapped. The distance between these points is determined from the latitudes and longitudes of the satellite grid points and those of the new higher resolution grid. The value computed for each new grid point is the distance weighted mean of all the satellite grid points. Thus, points outside a certain distance, or radius of influence, will prove negligible.

To determine this radius, a satellite image will be remapped into an equal resolution grid using a multitude of radii. Since only points whose distance is less than or equal to the specified radius will be used to calculate the value of each new grid element, changing the radius essentially changes the number of values used in the weighted mean computation. Thus, the value assigned to each new grid point will vary according to the radius of influence used. The radius producing an image most similar to the original will be chosen as the optimum radius of influence.

To see which radius provides the best estimate of the

original image, the new image will be compared to the original on a grid point basis. Here, the difference between grid point values for each remapping will be used to compute the root mean square error (RMSE) resulting from the applied radius of influence. The radius of influence which minimizes the RMSE is deemed the optimum radius and will be utilized in the remapping process.

After determining the optimum radius of influence, a computer optimization of the correlation coefficient, relating vertically averaged horizontal radar reflectivities and digital infrared counts of GOES images, will be performed. This essentially involves positioning the DBZ image at several different places within the satellite image, calculating the correlation coefficients, and selecting the optimal position as the one with the highest correlation coefficient. In order to avoid the problems associated with local maxima/minima, this process will employ a twenty five point search at each stage of the optimization process.

To initiate the search, the relative latitudinal and longitudinal offsets between the center points of the infrared and reflectivity grids will be determined. With this as a reference, an array of twenty five offsets, symmetrically located about the center point offset, are calculated and used as the initial offset matrix. Using each of these offsets, the satellite image will be mapped into the high resolution reflectivity grid, and a correlation coefficient

Table 1. Cases Studied and Sample Identifiers

| Case | Time | <u>Cloud Type</u> | <u>Sample Id</u> |
|-------------|-------------|-------------------|------------------|
| July12,1990 | 03:24-03:36 | convective | July12A |
| | 03:36-03:50 | stratiform | July12B |
| | 04:50-05:06 | stratiform | July12C |
| July17,1990 | 20:36-20:50 | convective | July17A |
| | 21:08-21:15 | convective | July17B |
| | 22:44-22:51 | stratiform | July17C |
| July20,1990 | 02:43-02:58 | convective | July20A |
| | 03:00-03:35 | convective | July20B |
| | 04:20-04:35 | stratiform | July20C |

Table 1. Cases Studied and Sample Identifiers

List of internal reflectivity samples used by day of storm and type of cloud region viewed. Duration of radar observation and sample identifiers are also included.

will be calculated. The offset having the highest correlation is then moved to the center of the offset matrix, new symmetric offsets are loaded, and another mapping and correlation follows. This process will be repeated until no further improvement in the correlation coefficient is found.

Once the optimization has been performed, visual inspection of the results, and determination of the net reflectivity grid movement, will be used to assess the integrity of the optimization process. The necessity of the

grid realignment stems from combined P-3 and satellite navigational errors, which make collocation according to center point offsets insufficient for correct alignment of the DBZ and IR reference frames.

Satellite navigational errors result from transmission of incorrect orbit and attitude information for the image and parallax. Parallax is the erroneous positioning of a cloud top relative to the ground due to the satellites non-vertical viewing angle. Orbit and attitude errors are common to most images, whereas parallax is only important when viewing tall clouds obliquely (Schlatter, 1986). Thus, parallax errors must be contended with when considering satellite images of convective storms, whose vertical depths can reach upwards of 18 km. For the mesoscale convective systems considered in this study the average parallax error is computed in the following example.

EXAMPLE 1.

$$PE = \left(\frac{h \times \sin(z)}{\cos(z)} \right) \quad (\text{Schlatter, 1986})$$

where

$$z = \arccos [\sin \phi \sin d + \cos \phi \cos d \cos H]$$

and

PE = Parallax Error

z = zenith angle

h = height of anvil clouds

d = satellite declination angle

phi = latitude of storm

H = (i.e. storm longitude - satellite longitude)

$$z = \arccos \left[0 + \cos(28) \cos(0) \cos(9) \right] = 29.29 \text{ deg}$$

$$PE = \left(\frac{17 \text{ km} \times \sin 29.3}{\cos 29.3} \right) = 9.5 \text{ km}$$

During SWAMP, the geosynchronous satellite was positioned over the equator at a longitude of -99.0W (SWAMP, 1991). With average storm position taken as 28N, -108.0W and average cloud top height assumed to be 17 km, the average parallax error for the systems used in this study is 9.5 km. Combined parallax, orbit and attitude errors can be as large as 30km (Schlatter, 1986).

Along with satellite positioning errors, P-3 navigational errors are also important. P-3 positioning errors typically result from inertial drift and the Schuler oscillation. The Schuler oscillation results from precession of the gyroscopes utilized by the inertial navigation system (INS) of the NOAA P-3 aircraft. Inertial drift, on the other

hand, is generally attributed to mechanical imperfections of the INS gyro's, poor calibration of the INS, and deficiencies in its computer algorithms (see Masters and Leise, 1990 for more thorough discussion). Masters and Leise indicate the Schuler oscillation typically results in position errors on the order of 1-7 km, while inertial drift errors tend to grow exponentially and can accumulate at rates of 2-7 km per hour. In most cases, inertial drift is corrected from terminal position information, where terminal errors are distributed linearly across the duration of the flight. However, this can only be done with the aid of Loran-C navigational beacons. These provide the aircraft with a fixed reference point from which navigational errors can be determined and corrected for. Unfortunately for SWAMP, Loran-C coverage was unavailable and thus terminal correction for inertial drift was not possible for these flights (Phil Bogert, SWAMP Flight Director, personnel communication). Errors due to the Schuler oscillation are not affected by terminal corrections (Masters and Leise, 1990).

Following optimization of the correlation coefficient as described above, the final aspect the first portion of this analysis will be a linear regression in which internal radar reflectivities will be dependent on digital IR counts. This will establish a working relationship between the digital IR counts and internal radar reflectivities of each sample listed in Table 1. These regression equations will

be of the form illustrated by equation 1. With digital IR counts as the independent variable, it will now be possible to estimate internal radar reflectivities from pixel values of infrared satellite images.

$$DBZ = Slope \times (IR - \overline{IR}) + \overline{DBZ} \quad (1)$$

3.2 Regression Line Combination

Assuming a positive linear relation between digital infrared counts and internal reflectivity values is found, the regression lines for each sample will be compared by case and type (convective vs. stratiform) using a method described by Brownlee (1965). This analysis will attempt to determine: 1) whether the regression lines of each case may be combined into one regression line; 2) if regression lines of a common type within a case can be combined; 3) if the regression lines representing stratiform or convective types may be combined across cases; and 4) if all regression lines can be combined into one regression line.

Using Brownlee's methodology it is first necessary to determine if the variances of the separate observations can be considered estimates of a common variance. The combination of several least squares lines is only possible if this is true. Secondly, it must be determined if the slopes

of the individual regression lines are significantly different from the average slope of the separate lines. If they are, then the analysis is complete. The lines can not be regarded as coincident if their slopes vary significantly from the mean slope. Otherwise, the analysis continues by testing the hypothesis that the group means all lie on the least squares line representing the true population. If the group means do not lie on this line, then the separate lines are not representative of the true population. However, if it is accepted that the group means do lie on the least squares line, then the possibility that the individual regression lines are coincident is evaluated. Acceptance of the coincidence hypothesis implies that the composite regression line is an adequate fit for all populations involved.

Attempts to combine regression lines will determine if any relationship between the internal reflectivities and digital IR counts (or cloud top temperatures) of one sample are common to other samples of the same type. If the regression lines are similar and can be combined, then a universal relationship between internal reflectivities and cloud top temperatures of convective, or stratiform regions may exist. On the other hand, no similarities would imply that any relation between cloud top temperature and reflectivity are unique to each system or the climatology of the day.

3.3 Daily Rainfall Estimation

The final phase of this analysis will estimate daily surface precipitation over a 720x720 km² area using hourly GOES infrared images and the regression equations derived earlier. With these equations, an internal radar reflectivity field is generated for each hourly infrared image. This provides a DBZ value for each grid point in the analysis domain. To estimate surface rainfall, the reflectivity value of each grid point is used as input into a reflectivity-rainrate relation. This produces an hourly surface rainrate field from which daily rain volumes are computed. However, in order to generate rain fields it must be determined which grid points are actively precipitating and whether this rainfall is convective or stratiform in nature.

To discriminate between raining, or non-raining, and convective, or stratiform, precipitation regions, a method used in the Convective-Stratiform rainfall estimation Technique (CST) of Adler and Negri (1987) will be employed. Following conversion of digital IR counts to cloud top temperatures, this technique identifies raining clouds through calculation of a slope parameter, S , defined as the difference between the temperature of the grid point in question, $T_{i,j}$, and the average temperature of six surrounding pixels. Or, in other words,

$$S = \bar{T}_{1-6} - T_{i,j} \quad (2)$$

where

$$\bar{T}_{1-6} = \frac{(T_{i-2,j} + T_{i-1,j} + T_{i+1,j} + T_{i+2,j} + T_{i,j+1} + T_{i,j-1})}{6.0} \quad (3)$$

if the current position is i, j . To account for parallax distortions, Adler and Negri have chosen \bar{T}_{1-6} so that it is not the average of the six closest pixels. Instead, the north/south offset is half as large as the east/west offset. To determine if rain is likely for a particular $T_{i,j}$, S is computed and compared to an empirical slope parameter determined by analysis of August thunderstorms for a Florida region centered near 26N, 81W. The empirical slope parameter, S_e , of Adler and Negri is given by

$$S_e = 0.568 \times (T_{i,j} - 217.0). \quad (4)$$

Grid points whose slope parameter is greater than S_e are considered to be regions of active precipitation. Otherwise they are classified as thin(nonraining) cirrus, or no cloud, and are ignored. Because the constants of this relation were determined in a different climatological regime some attention will be given to questions concerning its

transportability to Mexico.

Although the climates of Florida and Mexico are very different on an annual basis, they are not distinctly different during the summer season. Comparison of August climate in Florida to the July climate of Mexico (all case studies of this analysis occurred in July) indicate two regions with similar vertical temperature and moisture profiles. Mean monthly dew point temperature at the surface is slightly higher in Florida ($20^{\circ} \text{C} \leq T_d \leq 24^{\circ} \text{C}$) than in Mexico ($16^{\circ} \text{C} \leq T_d \leq 24^{\circ} \text{C}$), while surface temperatures are higher in Mexico ($24^{\circ} \text{C} \leq T \leq 32^{\circ} \text{C}$) than in Florida ($24^{\circ} \text{C} \leq T_d \leq 29^{\circ} \text{C}$). At 850mb Mexico is still warmer ($T_M \sim 23^{\circ} \text{C}$, $T_F \sim 17^{\circ} \text{C}$) but both sites have approximately the same T_d ($\sim 12^{\circ} \text{C}$). However, at 700 mb the mean T_d of Mexico is larger than that of Florida ($T_{dM} \sim 3^{\circ} \text{C}$, $T_{dF} \sim 1^{\circ} \text{C}$), while the ambient temperature is still higher over Mexico ($T_M \sim 10^{\circ} \text{C}$, $T_F \sim 8^{\circ} \text{C}$). The trend for higher ambient temperatures over Mexico ends at 500mb where both sites have a mean temperature of approximately -7°C . On the other hand, Mexico still has more water vapor available ($T_{dM} \sim -15^{\circ} \text{C}$, $T_{dF} \sim -17^{\circ} \text{C}$). Thus, it appears that Florida has slightly more moisture near the surface while Mexico displays more at middle to upper levels. Overall, the vertical distribution of temperature and moisture over Florida in August, are not significantly different from those over Mexico in July, and it is felt that use of the generic slope parameter over Mexico would not result in

considerable discrepancies. Furthermore, estimating the mean monthly height and temperature of the tropopause from the mean monthly 200mb geopotential height (GPH) and temperature over the two regions, shows that tropopausal heights and temperatures are nearly the same ($GPH_M \sim 12440\text{gpm}$, $GPH_F \sim 12400\text{gpm}$, and $T_M \sim -54^\circ\text{C}$, $T_F \sim -55^\circ\text{C}$), such that cloud top temperatures of anvils reaching the tropopause would be approximately equal. Numbers used in the above discussion were extracted from a government document prepared by Crutcher and Meserve, 1966.

Once a grid point has been identified as raining it must now be labeled either convective or stratiform in nature. This procedure initially treats all raining points as convective and then looks closely at those points whose slope parameter is less than or equal to 4.0. For each of these stratiform candidates, a modal temperature, or temperature that occurs with the highest frequency, is computed for a region $\sim 80\text{km}$ on a side and centered on each $T_{i,j}$. In order to eliminate ground effects only grid points with $T_{i,j} < -20^\circ\text{C}$ are included in the mode calculation. After the modal temperatures have been determined, segregation of these temperatures into one degree Celsius $T_{\text{mode}(i)}$ bins, ranging from -20°C to -80°C , will take place. The stratiform temperature threshold, T_s , is then computed as the weighted mean $T_{\text{mode}(i)}$,

$$T_s = \frac{\sum_{i=1}^k (T_{mode(i)} \times W_i)}{\sum_{i=1}^k W_i} \quad (5)$$

where W_i is the number of stratiform candidates with temperature $T_{mode(i)}$. All grid points passing the precipitation test with a slope less than or equal to 4 and a temperature greater than T_s will be treated as stratiform. Those with temperature less than T_s will be considered as convective precipitation (Adler and Negri, 1987).

Having determined precipitating convective and stratiform grid points, surface rainfall will be estimated through use of the derived regression equations. Specific examples of the operative equations will depend on the results of the regression analysis. These equations will be applied to hourly GOES images corresponding to the 24 hour period of daily surface rainfall observations. Application of the least squares equations to hourly infrared images will produce hourly horizontal reflectivity fields representing the vertically averaged horizontal reflectivities of the clouds in question. In order to produce the corresponding surface rainfall distributions, these reflectivities will serve as input to $Z = 55R^{1.6}$, the regionally tuned reflectivity-rainrate relation used by the National Weather Service in Tucson. It is felt that precipitation estimates may be im-

proved using this local ZR relation instead of the more general Marshall-Palmer relation commonly used by other researchers. Daily rainfall totals for the selected areas will be obtained from the hourly rain rate fields using three different rainfall estimation techniques.

Since the hourly rain volume assigned to any grid point is simply the product of the rainrate(mm hr^{-1}), the area of the grid square(mm^2), and the length of the precipitation interval(1 hr), the first rainfall estimation technique will produce a daily volumetric rainfall amount by simply summing the hourly rain volumes over all grid points and hourly time intervals. No consideration is given to the overall echo area. This method will henceforth be referred to as the grid point approach.

The second rainfall estimation technique is also an area-time integral approach, but instead of accumulating rainfall on a grid point by grid point basis, this method estimates daily rain volumes, V , by multiplying a slope parameter, $S(t)$, with the area-time integral(ATI). The ATI is the product of the time interval(24 hrs) and the average area, $A(t)$, where precipitation is greater than or equal to an optimal rainfall threshold, t . Therefore, this method will be referred to as the ATI approach, where daily rainfall is determined using the following formula:

$$V = S(t) \times [A(t) \times T] = S(t) \times ATI \quad (6)$$

(Atlas, Rosenfeld, and Short, 1990). Both t and $S(t)$ will be determined empirically using the nine vertically averaged horizontal reflectivity grids described earlier, and the local ZR relationship.

To calculate $S(t)$ and t , the average areawide rainrate, R , for each radar image must first be determined. This is computed as the ratio of the volumetric rainfall rate to the total precipitation area. The volumetric rainrate for each image is the sum of all grid point volume rainrates, where each grid point volume rainrate is the product of the area represented by that point and the instantaneous rainrate assigned to it with the applied ZR relation. Since the areal distribution of rainrates will be different for each radar image, the volumetric rainrate, and therefore, the average areawide rainrate will also be unique.

Although R is determined using grid point summations as in the previous approach, this method is distinct from the grid point approach in that, the slope parameter is calculated from actual reflectivity data, not estimated reflectivity fields. Therefore, no summation of rain volumes associated with the estimated reflectivities will occur with the ATI approach. Only the areal distribution of

rainrates derived from the estimated reflectivity fields will be used in determining rainfall volumes. The grid point method, on the other hand, obtains its rain volume estimate entirely from the rain volumes generated using the estimated reflectivity fields.

Once R is determined for a particular DBZ image, slope parameters, $S(t_i)$, and fractions of the total precipitation area, $F(t_i)$, with rainrates greater than or equal to specific rainrate thresholds, t_i , are calculated for various rainfall thresholds. These thresholds are chosen in 1 mm hr^{-1} increments. Since the average areawide rainrate is constant for any instantaneous radar reflectivity or rainfall snapshot, it can be written that

$$R = S(t_i) \times F(t_i), \quad i = 1, 2, \dots, n \quad (7)$$

for each of the nine DBZ images employed in this study (Atlas, Rosenfeld, and Short, 1990). Therefore, as fractional coverage decreases the slope parameter must increase to provide the same average areawide rainrate. Thus, for each reflectivity image there will be an R , $F(t_i)$ pair corresponding to each rainrate threshold t_i .

After compilation of these statistics for each of the nine reflectivity samples, a linear regression is performed for each rainfall threshold using the R and $F(t_i)$ pairs

from each image, where $F(t_i)$ is the independent variable. This will produce a regression line with a distinct slope for each rainfall threshold evaluated. The slope of the regression equation indicating the highest correlation is designated as the slope parameter, $S(t)$, and the corresponding rainfall threshold is deemed the optimal threshold, t . It is this rainrate threshold which will determine the precipitation area to be used in the ATI volumetric rainfall estimation.

An alternative method of computing the slope parameter involves the population distribution of the rainrates. Rosenfeld, Atlas, and Short(1990) show that $S(t)$, determined through linear regression analysis of R and $F(t_i)$ pairs from hundreds of radar scans, compares favorably with $S(t)$ obtained from the probability density function(pdf) of the rainrates, as illustrated in equation 8, where $P(r)$ is defined as the percentage of the precipitation area where the rainrate is between r and $r+dr$.

$$S(t) = \frac{\int_0^{\infty} rP(r) dr}{\int_t^{\infty} P(r) dr} \quad (8)$$

However, such behavior depends on the observed area being large enough to provide rainrates representative of the

true population distribution. This means that there must be a minimum number of cells (~30) in an observing area larger than 10^4 to 10^5 km² (Rosenfeld, Atlas, and Short, 1990). Atlas, Rosenfeld, and Short further indicate that $S(t)$ obtained from the distribution of rainrates produced by an individual convective storm over its lifetime is equivalent to the $S(t)$ obtained from the distribution of rainrates provided by an instantaneous or snapshot view of a multitude of storms in various stages of development. Thus there is an inherent space-time trade off in this approach.

In this analysis, however, neither of these conditions are met as the $S(t)$ will be determined from rainfall distributions estimated from three random radar snapshots within three distinct convective systems. It is felt that these random high resolution images, when considered together, contain enough cell samples in varying stages of development to provide a snapshot which will give a representative probability distribution for the rainrates. Therefore, comparison of the slope parameters obtained through linear regression of R and $F(t_i)$ pairs from each DBZ image, and $S(t)$ determined from the probability distribution of the rainrates, will provide an indication of the validity of this application of the area-time integral.

The final method of estimating volumetric rainfall is better known as the Height-Area Rainfall Threshold (HART) method. This technique is similar to the area-time integral

approach of Atlas, Rosenfeld, and Short. However, in this scheme, the efficiency of precipitation mechanisms within a particular climatic regime is taken into account. Computation of the slope parameter no longer results from the regression of R against $F(t_i)$, but instead is derived through a regression of $[E_e(t_i) \times R]$ on $F(t_i)$, where $E_e(t_i)$ is the effective precipitation efficiency for each rainfall threshold. This parameter tends to reduce $S(t)$, and thus, volumetric rainfall in accord with decreased surface precipitation resulting from evaporation, entrainment, and mixing (Rosenfeld, Atlas, and Short, 1990). The effective efficiency parameters can be determined for each rainrate threshold from

$$E_e = \frac{(Q_b - Q_t)}{Q_b}, \quad (9)$$

where Q_b and Q_t are the mixing ratios at cloud base and top, respectively. Utilization of efficiency parameters involves creating a table of precipitation efficiencies verses rainrate thresholds. This requires computation of the precipitation efficiency for each grid point and thus, both cloud base and cloud top heights must be known at each grid point. Due to the unavailability of cloud base information on a grid point basis, the precipitation efficiencies to be used in this analysis are those derived for sum-

mer in Big Springs Texas and presented by Rosenfeld, Atlas, and Short(1990). The choice of the Texas precipitation efficiencies over the Florida(GATE) efficiencies was due to the proximity of Texas to Mexico, and the fact that both of these climatological regimes appear to be influenced by moisture fluxes from the Gulf of Mexico during the summertime monsoon period. However, the choice of efficiency parameters could be used to influence results of the rainfall analysis. This was not the case in this study.

4. Results of Correlation and Regression Analysis

Before performing the correlation and regression analysis, an optimum radius of influence was chosen for mapping the lower resolution IR images into the higher resolution reflectivity space. Incorporated into the Cressman weighting scheme, the radius of influence determines which grid point values of the lower resolution IR grid are used to calculate the grid point values of the new, higher resolution IR grid. By mapping a given satellite image into an equal resolution grid with varying radii, the optimum radius of influence was chosen as the one which minimized the root mean square error(RMSE) between the new IR image and the original IR image, or in other words, the optimum radius was that which produced an image most like the original. Minimum RMSE was found for a radius of 0.1 degrees latitude, or approximately 11 km assuming a spherical

earth. Using this radius, a RMSE of 2.67 with a negative bias of 0.082 digital IR counts was found, implying that some degree of smoothing occurred during remapping and resulted in slightly lower IR values.

Having determined the optimum radius of influence the correlation optimization and regression analysis were performed as described earlier. As previously stated, correlation coefficients were determined using vertically averaged horizontal reflectivities. It was felt that these would provide a more representative sample, since early correlation attempts using the average of the correlation coefficients from sixteen reflectivity levels were poor. Although some levels displayed high correlations, other levels displayed low or negative correlations and the two tended to cancel. This effect is consistent with earlier descriptions of the multicell, meso-beta scale, and meso-alpha scale convective systems.

Table 2 presents correlation and regression results, while Table 3 displays the resulting regression equations. Corresponding regression lines are presented in Figure 3. Aside from listing correlation coefficients, slopes of the regression lines, net grid movement, and the regression variances for each sample, Table 2 also contains some items which require additional discussion.

In an attempt to better identify any patterns emerging from the correlation and regression results, additional

statistics for both the infrared and reflectivity samples were included in Table 2. For each sample the standard deviation and covariance were computed for the IR and DBZ values used in the regression analysis. Since the internal reflectivity fields were spatially limited by the wavelength of the P-3 tail radar and the period of observation, some points in the reflectivity grid had DBZ values equal to zero. These points were not used in the analysis as it was uncertain whether the zero value resulted from attenuation, lack of echo, or lack of radar observation. Therefore, since the IR and DBZ images were on identical grids once correlation began, the statistics listed in Table 2 are those computed from grid points with non-zero reflectivities.

Another topic requiring special mention is that of degrees of freedom. The assignment of degrees of freedom depends on the number of independent pieces of information available for the decision making process. For a typical correlation or regression analysis it is assumed that the values entering into the computations are independent, and therefore, the number of degrees of freedom are equal to the number of points utilized minus one or two, respectively. In this analysis, however, the determination of degrees of freedom is not so trivial.

First of all, there is the problem of different resolutions between the two data sets. With the horizontal reso-

lution of the infrared and reflectivity grids being, 8 km and 3 km, respectively, there will be a different number of points representing the same grid space. Thus, the number of degrees of freedom for each image will not be the same.

Table 2. Correlation and Regression Results

| Sample | Net Offset | Type | Corr. Coef(r) | 95% CI | Slope (b) | Degrees Freedom | Covar | Std. Dev. | | Reg. Var.(s ²) |
|---------|---------------|------|------------------|-----------|--------------|--------------------|--------|-----------|-------|-------------------------------|
| | | | | | | | | DBZ | IR | |
| July12B | 51.11 km | S | 0.815 | .80-.84 | 2.47 | 4-14 | 10.04 | 6.11 | 2.02 | 12.52 |
| July12C | 56.63 | S | 0.708 | .68-.74 | 1.38 | 5-17 | 21.36 | 7.67 | 3.93 | 29.38 |
| July20C | 80.76 | S | 0.600 | .57-.63 | 0.80 | 6-22 | 30.30 | 8.20 | 6.16 | 42.97 |
| July17A | 10.12 | C | 0.584 | .54-.62 | 0.26 | 3-12 | 108.35 | 9.14 | 20.31 | 55.05 |
| July17B | 17.39 | C | 0.576 | .53-.63 | 0.24 | 2- 8 | 95.97 | 8.37 | 19.93 | 46.73 |
| July20A | 14.98 | C | 0.531 | .49-.57 | 0.19 | 4-14 | 183.01 | 11.04 | 31.22 | 87.60 |
| July12A | 33.84 | C | 0.507 | .48-.54 | 1.64 | 7-24 | 11.49 | 8.56 | 2.65 | 54.51 |
| July20B | 26.50 | C | 0.339 | .29-.39 | 0.01 | 4-16 | 125.71 | 10.43 | 35.53 | 96.33 |
| July17C | 18.22 | S | 0.314 | .25-.37 | 0.25 | 3-12 | 29.53 | 8.67 | 10.85 | 67.79 |

Table 2 - Correlation and Regression Results.

Includes distance DBZ grid moved within IR grid to maximize correlation(net offset), type of cloud sampled, C(convective), or S(stratiform), correlation coefficient(r), 95% confidence interval(CI) for the correlation coefficient, slope of regression line(b), range of degrees of freedom(from IR to DBZ values), IR and DBZ covariance, standard deviation of IR and DBZ values within individual IR and DBZ fields of each case, and the regression variance(s²). All entries are organized in the descending order of their respective correlation coefficients.

Secondly, both images display some degree of spatial correlation among their component grid points. In this case, the IR or DBZ value at a particular grid point is not independent of its neighbors and therefore, the number of de-

degrees of freedom for each image can not be equal to the number of points within that image.

As a result, the number of degrees of freedom are felt to be some function of the number of DBZ grid points that map

Table 3. Regression Equations

| <u>Sample</u> | <u>Eqn. No.</u> | <u>Least Squares Regression Lines</u> | <u>RMSE (DBZ)</u> |
|---------------|-----------------|---------------------------------------|-------------------|
| July12A | 12a | DBZ=1.64(IR-212.02)+19.74 | 4.38 |
| July12B | 12b | DBZ=2.47(IR-211.07)+22.05 | 1.55 |
| July12C | 12c | DBZ=1.38(IR-208.05)+20.21 | 2.64 |
| July17A | 17a | DBZ=0.26(IR-174.91)+25.81 | 3.03 |
| July17B | 17b | DBZ=0.24(IR-189.70)+24.56 | 2.32 |
| July17C | 17c | DBZ=0.25(IR-194.50)+18.67 | 3.48 |
| July20A | 20a | DBZ=0.18(IR-178.08)+24.09 | 4.17 |
| July20B | 20b | DBZ=0.10(IR-173.29)+22.87 | 4.87 |
| July20C | 20c | DBZ=0.80(IR-206.83)+18.26 | 3.71 |

Table 3. Regression Equations.

Includes regression equations for each DBZ and IR image pairing. RMSE is the root mean square error resulting from the comparison of the actual vertically averaged horizontal reflectivity field to the reflectivity field generated by application of the regression lines to the appropriate satellite infrared image.

into one IR grid point and the number of degrees of freedom in each grid. Accordingly, degrees of freedom were estimated by determining the number of grid points surrounding any particular point and showing a correlation of 50% or greater. The corresponding number of degrees of freedom was then obtained by dividing the number of non-zero grid

points used in the regression analysis by this number. This was performed separately on the vertically averaged horizontal reflectivity grids and the corresponding optimum infrared shields presented in Figure 1. The optimized infrared images were used as a means of eliminating the differing IR and DBZ spatial resolutions from the degrees of freedom estimation.

Overall, the reflectivity images displayed less spatial correlation than the infrared images, and as a result had more degrees of freedom. Computation of the correlation coefficient as a function of distance indicated that, on the average, IR and DBZ points lying within a radius of ~30 km, and ~15 km, respectively, showed correlations of 50% or greater. Thus, the number of spatially correlated IR and DBZ grid points within these circular areas were ~289, and ~81, respectively. Dividing the number of non-zero grid points by these resulted in a range of degrees of freedom for the infrared and reflectivity grids of 2 to 7, and 8 to 24, respectively. It is felt that the actual number of degrees of freedom for a particular regression will lie somewhere between those for the associated infrared and reflectivity images. These values are presented in Table 2.

Having discussed those aspects of the analysis which required further clarification, presentation of the correlation and regression results will proceed as follows. First of all, the net grid movement involved in producing the

highest correlation for each sample will be discussed. Secondly, any trends or anomalies evident in the regression and correlation statistics of Table 2 will be considered. Following this, the significance of the correlation coefficients and slopes of the regression lines will be examined. Finally, a paragraph or two will be dedicated to the use of the regression lines for internal reflectivity estimation from satellite infrared images.

As part of the correlation analysis, the IR and DBZ grids were moved relative to each other until the correlation coefficient was maximized. This was felt to correct the inherent positioning errors resulting from incorrect satellite and P-3 navigational information, provided that net grid movements were within reasonable bounds. Overall, the correlation coefficients resulting from the net grid movements were considerably higher than those obtained by simply aligning the IR and DBZ grids using only the center point offsets. These improvements ranged from 3% to 53% with 7 of 9 correlation coefficients increasing more than 23%. However, from consideration of Table 2, it is evident that three image realignments resulted in net grid movements in excess of 50 km. Due to the lack of Loran-C coverage during SWAMP, cumulative position errors of 51 km and 57 km between the satellite and P-3 navigation systems are considered possible. In fact, worst case scenarios of inertial drift errors accumulating at a rate of 7 km per hour

result in 42 km offsets for a six hour flight. Adding parallax, and orbit and attitude errors of approximately 10 km and 20 km, respectively, leads to a total position error of about 70 km! However, the 81 km offset of JULY20C is still seen as excessive and is felt to be the result of anomalous navigational errors.

Inspection of hourly GOES images pertaining to the July20 system and presented in Figure 2, show that this stratiform region essentially develops from the northwestern convective elements after 0300 UTC. However, this development takes place nearly due west of the earlier convective cloud tops(0300 UTC) such that very little southerly movement(~ 0.2 degrees latitude or ~ 22 km) of the cloud shield is evident from 0300 to 0400 UTC. Yet, the displacement of the processed reflectivity shield, from 0310 to 0428 UTC(Fig. 1), is approximately 67 km to the southwest. Subtraction of this additional 45 km($67 - 22$ km) from the computed offset of 84 km results in a net grid movement of 39 km, clearly within reasonable error bounds.

Visual verification of the optimized positions can be obtained through examination of the contoured reflectivity images and corresponding optimal infrared images presented in Figure 1. These alignments appear reasonable for the magnitude of the correlation coefficients listed in Table 2, and display no large disparities except for July20A and July20B. The correlation maximization process in these

cases appears to have placed the images too far to the northeast, such that areas of high reflectivity extend into tight infrared gradients. However, manual placement of the DBZ images toward the southeast or center of the high IR regions resulted in lower correlations. Furthermore, wide area local maximum studies displayed a trend of the highest correlations in this sector.

Collocation of the other IR and DBZ images, especially the samples of July17, indicate considerable agreement with the correlation and regression results. Positive correlations between IR and DBZ values are evident, most notably among stratiform samples. Although the high reflectivity cores in July12B and July12C appear out of place, they are but a few anomalous points among many which display stronger associations and therefore, the correlations between these grids remain high. For July17C, on the other hand, the overall placement of the DBZ image within the IR image seems valid and quite good, yet the correlation coefficient in this case is quite bad, in fact, it is the worst. Closer inspection reveals a wide variation of reflectivity values within the 190 IR contour. Here, DBZ values range from approximately 10 to 40 inside this contour, while IR values range from 190 to 206. Thus, the low correlation in this case seems appropriate.

Having discussed the net grid movements providing the highest correlations, the next topic of this section exam-

ines statistical patterns and anomalies found in the correlation and regression results presented in Table 2. Recalling that the convective or stratiform nature of each sample was determined by in-flight observers using on-board radar, it appears that the stratiform samples, in general, have lower IR and DBZ variances and covariances than the convective samples. This is not surprising, as internal reflectivity fields of convective regions are generally a composition of radar echoes with varying heights, vertical extents, and magnitudes, whereas stratiform regions consist of a more homogeneous reflectivity field (Smull and Houze, 1987; Gamache and Houze, 1985 and 1981; Schuur, 1991). This results from vastly different vertical motion fields within the two cloud types. Dominated in some cases by a middle level mesoscale low, stratiform regions of tropical squall systems generally have horizontally uniform vertical motions. The vertical motion of parcels in convective regions, on the other hand, is far from homogeneous and typically consists of several deep convective cells penetrating the equilibrium level and surrounded by shallower more benign convective elements. As a result, the reflectivity and infrared fields of convective clouds display considerable topography and therefore, a high degree of spatial variability, while the corresponding stratiform fields are smoother and more consistent (Smull and Houze, 1984 and 1987; Gamache and Houze, 1985 and 1981; Schuur, 1991).

Along with higher variances, the IR and DBZ values of the convective samples also display a larger covariance than those of the stratiform types. Although the covariance between two random variables gives qualitative information regarding the nature of the relationship, in this case positive, it does not indicate anything regarding the strength of that relationship (Walpole and Myers, 1988). Therefore, no attempt will be made to explain the magnitude of the covariances listed in Table 2. These numbers are merely presented to aid in the discussion that follows. Generally speaking, however, the larger covariances of the convective samples are felt to be a result of the greater range of IR and DBZ values found among these types.

In conjunction with variances and covariances that were lower than those of the convective types, the stratiform samples displayed larger correlation coefficients and regression line slopes. Since the correlation coefficient is the IR and DBZ covariance divided by the square root of the product of the IR and DBZ variances, the lower correlations among convective regions results from the greater spatial variability found in both the infrared and reflectivity samples of these types. This higher variability, and thus larger denominator for the correlation coefficient, outweighs the higher covariance common to the convective samples. Therefore, the high degree of spatial homogeneity found in the stratiform samples is primarily responsible

for the higher correlations. The anomalously low correlation for the July17C stratiform sample appears to be the consequence of the highest IR and DBZ variances found among the stratiform cases studied.

Although correlation coefficients of stratiform samples are generally higher than those for convective samples, neither imply a strong linear relationship. Squaring the correlation coefficient of each sample shows that in the best case 66% of the total variation of IR values is accounted for by their linear relationship with echo intensities. Only 10% of the variance is explained in the worst case.

Additional support for these conclusions comes from the scatter diagrams of Figure 3. These diagrams illustrate the strength of the linear relation through the compactness and linearity of the points. The stronger the linear relationship, the greater the tendency of the points to lie along a straight line, and the smaller the spread of the points about this line. The obvious feature of Figure 3 is the distinct difference in the nature of the convective and stratiform distributions. In the stratiform clouds, the linear relationship is most evident, with the spread of the points increasing as the correlation coefficient decreases. The convective regions, on the other hand, display a much wider scatter and therefore, a weaker linear relationship. In fact, the distribution of points pertaining to July20A

and July20B display an almost random character. The wider scatter evident in the convective samples is a result of the higher spatial variability found within both the IR and DBZ fields of these types.

In a manner similar to the correlation coefficient, stratiform cloud types had larger slopes than convective cloud types. Since the slope of the regression line is simply the covariance of the regression variables divided by the variance of the independent variable, which in this analysis was digital IR counts, the smaller slopes of the convective regression lines are also felt to result from the larger IR and DBZ variances found among these samples. However, two large disparities are indicated by the slopes listed in Table 2, and by the regression lines illustrated in Figure 3. In the convective case, July12A was found to have a slope almost one order of magnitude larger than the other convective types. In the stratiform case, the slope of July17C was almost one order of magnitude smaller than the other stratiform samples.

Although the in-flight observation technique discussed earlier indicates that July12A is of the convective variety, the statistics of July12A are more characteristic of the stratiform types. This is evident in the average IR(212.02) and DBZ(19.74) values for this case. These numbers are very similar to the average stratiform values(205.11, 19.78) and quite dissimilar to those of the

Figure 3. Scatter Diagrams

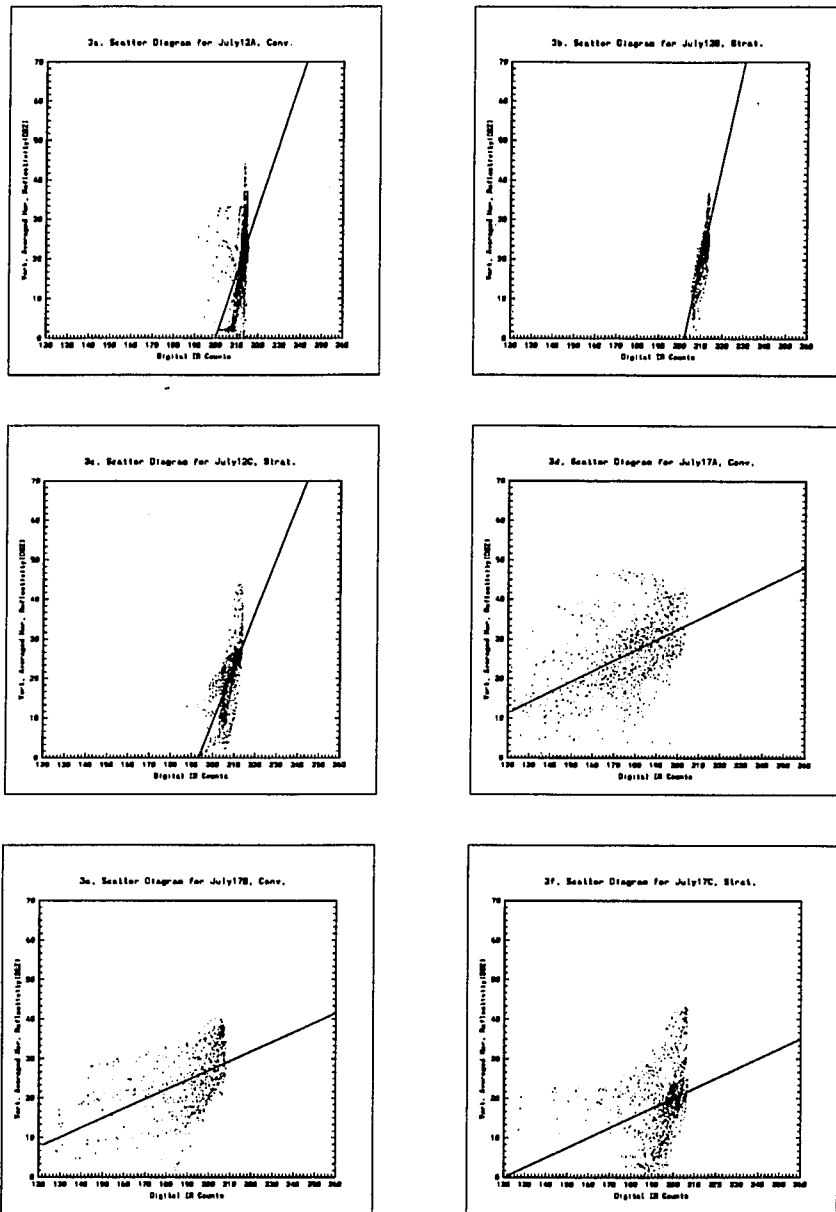


Figure 3 - Scatter diagrams.

Scatter diagrams for each IR-DBZ pair used in correlation and regression analysis.

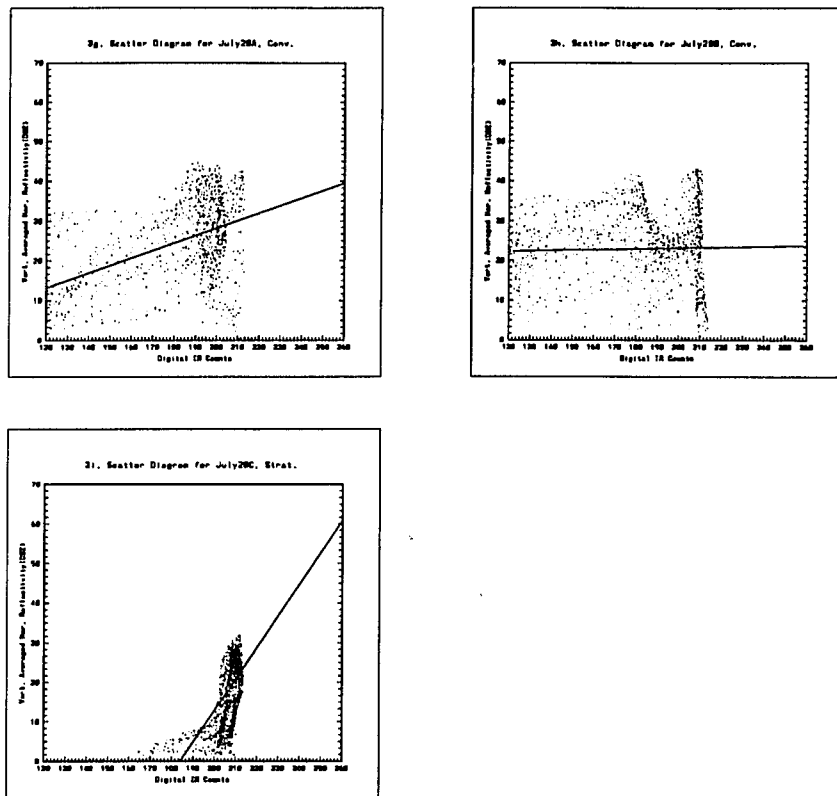


Figure 3 - Scatter Diagrams (cont)

convective types(185.6, 23.41). Even though the average DBZ value of July12A is more characteristic of the stratiform observations, its range of DBZ values(44.0) is more similar to the average range of the convective(43.4) observations than to the average range in the stratiform(38.5) regions. However, the range of IR values for July12A(24.0) is more characteristic of the stratiform ranges(46.3) than the convective(91.6) ranges. Additional stratiform features of

July12A are shown by its low covariance and by its scatter diagram in Figure 3, which clearly appears to have a point distribution more characteristic of the stratiform types.

In a manner similar to July12A, July17C appears to have more in common with convective samples, than with the stratiform samples in which it was included by in-flight observers. Along with the more convective slope of 0.25, closer inspection of the regression results for July17C indicates an average digital IR count(194.50) and range(100) which are more typical of the average IR value and range of the convective samples. Although the average DBZ value of July17C(18.67) is more characteristic of the stratiform observations, the range of its DBZ values(42.7) is more similar to the average range of the convective observations. Except for the covariance and the standard deviation of its infrared cloud shield, July17C appears statistically to be of the convective variety. This is not entirely surprising when considering the convective appearance, or cellular nature, of both the vertically averaged horizontal reflectivity field for July17C, as illustrated in Figure 1, and the corresponding infrared shield shown in Figure 2. Close inspection of the scatter diagram for this sample also seems to point to a convective classification.

Although positive correlation coefficients and slopes by themselves imply high digital IR counts are analogous to high internal reflectivities, it remains to be determined

whether or not these positive linear relationships have any statistical significance. Since significant positive regression line slopes indicate a significant linear relationship between two variables in the same manner as significant positive correlation coefficients, only tests involving the correlation coefficient will be discussed. The significance of the correlation coefficient for each sample was determined by evaluation of the null hypothesis, that no linear relationship existed between digital IR counts of satellite images and DBZ values of vertically averaged horizontal reflectivity fields. The alternative hypothesis, on the other hand, stated that a positive linear relationship did exist between the two. Testing the null hypothesis at the 5% level of significance using the one sided student-t distribution, results in a critical region for the alternative hypothesis of $t > t_{.95}(df_i)$, where df_i is the number of degrees of freedom for the i^{th} sample. In this analysis the number of degrees of freedom used for each sample was the average of the IR and DBZ degrees of freedom listed in Table 2.

Even though all correlation coefficients and regression line slopes were positive, it was found that these positive linear relationships were statistically significant in 3 out of 4 stratiform, and 3 out of 5 convective samples. Those samples showing nonsignificant linear relations included July17B, July17C, and July20B. As a result, it ap-

pears one can reasonably assume that high digital IR counts correspond to high internal reflectivities in stratiform regions of tropical MCS's. For convective regions, on the other hand, this assumption seems less valid. In fact, it was shown earlier that July17C, the non-significant stratiform sample, had statistics more characteristic of the convective types. Similarly, July12A, one of the significant convective samples, had statistics like those of the stratiform types. Thus, if these two samples are considered convective and stratiform, respectively, then 4 out of 4 stratiform samples exhibit significant positive relationships, while only 2 out of 5 convective relations are significant.

However, the two significant convective relationships, July17A and July20A, represent multicell and meso-beta MCS's, respectively, in the early stages of their lifecycles when individual convective elements are relatively distinct. The nonsignificant convective samples, on the other hand, represented regions where anvil mergers had begun such that individual convective elements were harder to identify. As a result, shallower, low level convective elements were obscured by high level cirrus and therefore, were undetectable by infrared sensors. Radar, however, can penetrate into the cloud and see these hidden cells. Thus, it seems reasonable that radar echoes and infrared images would display significantly different patterns in

convective regions of storms approaching the mature stage of development.

Therefore, since cold cloud tops have high digital IR values, it can be inferred that cold cloud tops correspond to high vertically averaged horizontal reflectivities for the stratiform samples used in this analysis. For convective samples, on the other hand, it appears this relationship is valid only in the developmental stage and decays significantly as storms reach the mature stage of their existence.

However, it must be remembered that statistical significance depends largely on degrees of freedom. Increasing the number of degrees of freedom actually improves the chance of rejecting the null hypothesis in favor of the alternative when using the student-t, or f distributions. Thus, underestimating degrees of freedom could turn a significant positive linear relationship into a nonsignificant one. In this analysis some uncertainty surrounded the choice of degrees of freedom and therefore, some must also surround conclusions involving the significance of the derived linear relationships.

Aside from comparing and contrasting the regression results in a purely statistical sense, use of the regression line for internal radar reflectivity estimation was also examined. Using only those infrared grid points corresponding to non-zero reflectivity grid points, the optimal in-

frared images utilized in the regression analysis now provided input for the regression equations derived for each sample. The resulting internal reflectivity fields generated are presented in Figure 4a-4i. Corresponding regression equations and RMSE between the actual and predicted reflectivity grids are listed in Table 3.

Visual inspection of the predicted reflectivity fields shows an overall smoothing of the radar returns yet higher reflectivity regions are still evident. One anticipated problem in these estimates is the occurrence of negative radar reflectivities on the fringe of some images. These negative regions correspond to areas where the actual reflectivity field extended into regions of strong IR gradients resulting in poor correlations. The negative values result from IR values which are less than the average IR value of the particular cloud shield. These regions will be tested for and removed during the rainfall estimation process.

Examination of the RMSE of prediction for each regression line indicates that prediction errors are negatively correlated with correlation coefficients. In other words, the RMSE of prediction increases as the correlation coefficient decreases. This is consistent with the the fact that higher correlations explain a greater portion of the variance of the IR and DBZ points about the least squares line, and as a result should correspond to better prediction equations.

Figure 4. Estimated Internal Reflectivity Fields

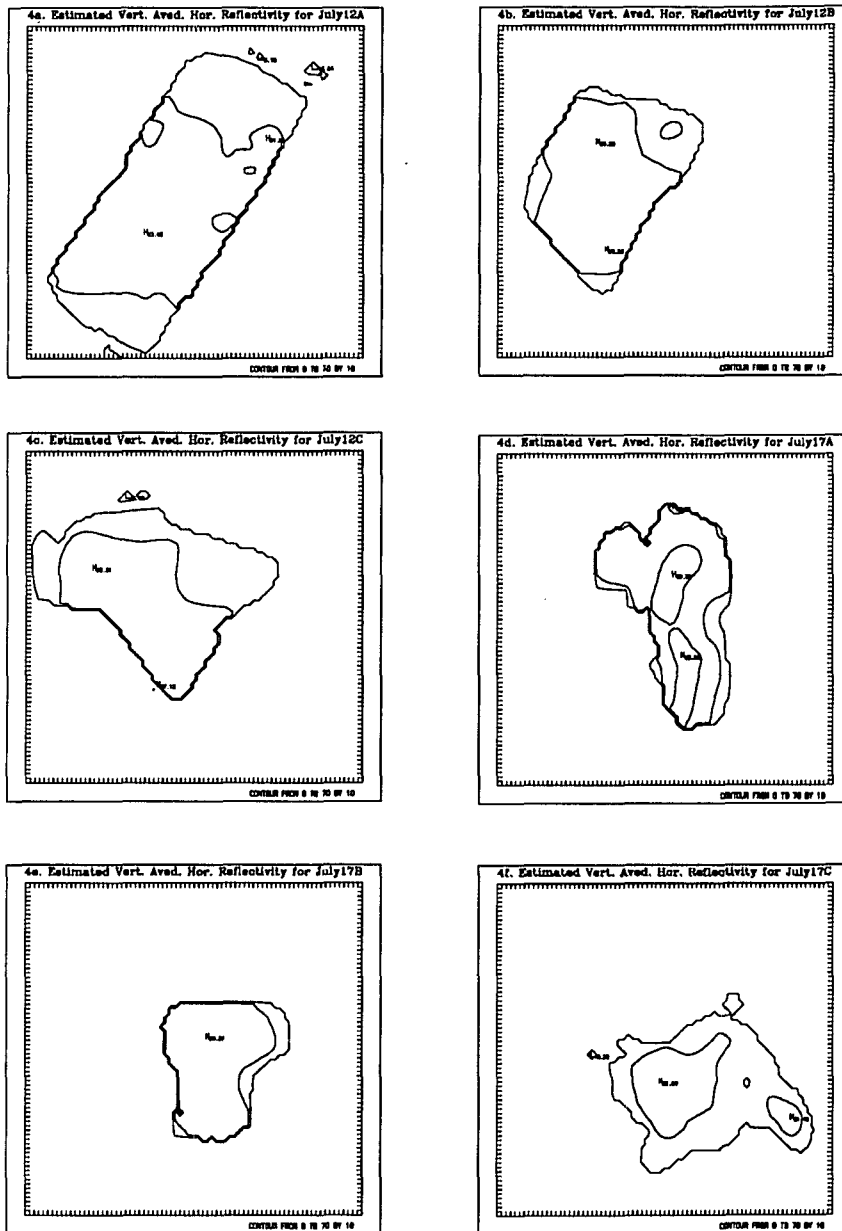


Figure 4. Estimated Internal Reflectivities.

Vertically Averaged Internal reflectivity fields generated using pixel values of GOES infrared subsectors as input into the regression equations derived in this analysis. Units are DBZ's. Tick marks represent 3 km increments.

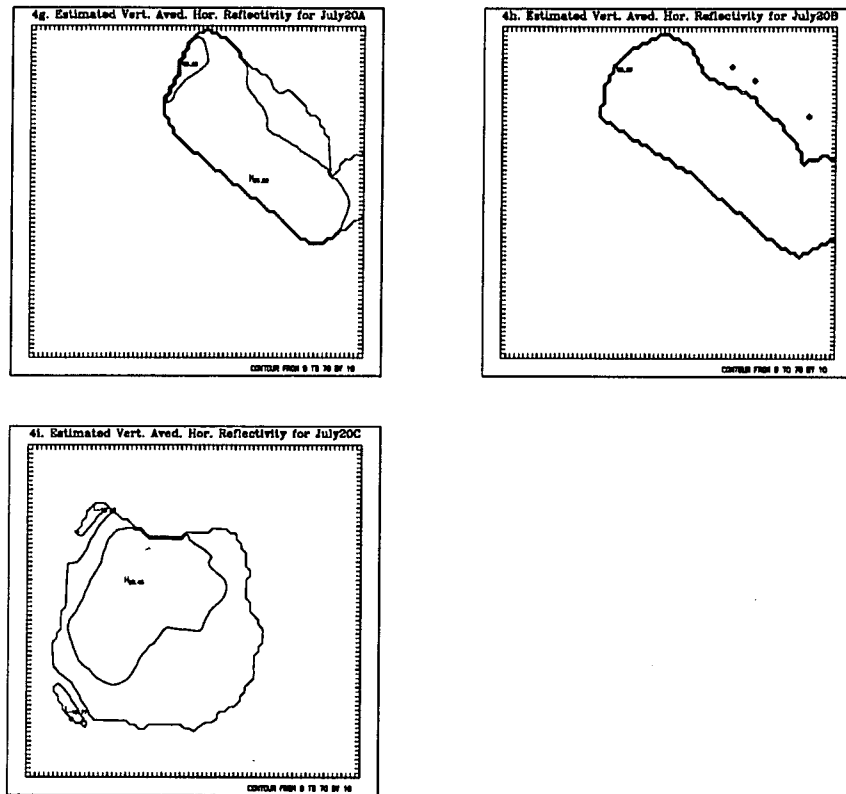


Figure 4. Estimated Vertically Averaged Horizontal Reflectivities.continued

5. Results of Regression Line Combination

Of particular interest in this analysis was the possibility of combining the regression line of one stratiform (convective) sample with other stratiform (convective) samples both within and across cases. Since the ability to combine regression lines implies considerable similarity between the two data sets involved, the ability to unite

regression lines from different sample environments would imply similar IR and DBZ populations and thus, a climatological relationship between these observations. Similarly, one could infer that a daily climatological relationship existed if the regression lines of both convective and stratiform samples taken from the same storm can be combined. In the same sense, synthesis of all samples of all storms would imply the existence of one regional infrared and internal reflectivity relationship. To evaluate each of these possibilities the regression lines being considered were put through a series of four hypothesis tests presented in Brownlee(1965). Failure of any of these tests would lead to immediate conclusion that these lines can not be combined in a statistical sense.

The first of these hypotheses tested if the variance of the points about the regression line of each sample being considered was an estimate of a common variance. This test proceeded under the null hypothesis that all regression variances being compared were equal to each other and the overall population variance, while the alternative states that they are not. The test statistic in this case is a chi-squared distribution and is distributed as $X^2(k - 1)$, where k is the number of variances being considered. This procedure is better known as Bartlett's test and is more thoroughly discussed in Brownlee(1965). Since each hypothesis in this series is simply looking to disprove the null

equality, a two-sided test will be performed for the evaluation of each.

Following Bartlett's test, the second hypothesis tested for significant differences between the slopes (b_i) of the individual regression lines and the average slope of these lines. Thus, the null hypothesis was $b_i = \text{ave. } b$ and the alternative suggests inequality between the two. To aid in this discussion the regression lines of all samples are illustrated in Figure 5. The test statistic for this hypothesis was distributed as $f(2, df_1)$ at the 5% level of significance where, df_1 represents the sum of the degrees of freedom for each slope participating in the combination attempt.

The third hypothesis tested whether the group means could be regarded as lying on a least squares line representing the true population. This was evaluated against the alternative that they do not lie on such a line using $f(1, df_1)$ at the 5% significance level, where df_1 is as indicated above.

The final hypothesis was evaluated using the same test statistic as the third. In this case, the null hypothesis of coincident regression lines was weighed against the alternative that the regression lines were not the same.

Before proceeding further it must be mentioned that the above four step procedure is only applicable to the combination of three or more regression lines. For combination

of two regression lines, a similar three step procedure as outlined in Brownlee(1965) will be employed. This methodology essentially uses the same variance, slope, and coincidence hypotheses discussed in the four step procedure. However, this process omits the third, or group mean hypothesis, and uses different test statistics to evaluate each of the remaining three.

To evaluate the similarity of two variances, the test statistic employed is simply the ratio of the larger to the smaller regression variance(i.e. s_1^2/s_2^2) for the two regression lines being considered. This is distributed as $f(df_1,df_2)$. Evaluation of the equal slope hypothesis is performed using the student-t test, where t is distributed as $t(df_1+df_2)$. Coincidence of the two lines being compared is also determined using the student-t, but in this case there are df_1+df_2+1 degrees of freedom. Each of these hypotheses will be evaluated with a two sided test as before.

Following computation of the correlation coefficients and the least squares lines, combination of several regression lines proceeded using the methods described above. In general, four different types of combinations were studied. These consisted of comparing the regression lines representing similar cloud types, both within and across each of the three cases studied. Additionally, all regression lines derived for a particular storm were compared and all regression lines from all three cases were compared.

Analysis of these possible combinations began with attempting to combine the two regression equations representing the same cloud types within each of the three storms studied. Thus, regression lines 12b and 12c, of Table 3, were compared for the system studied on July 12th, while

Figure 5. Regression Lines

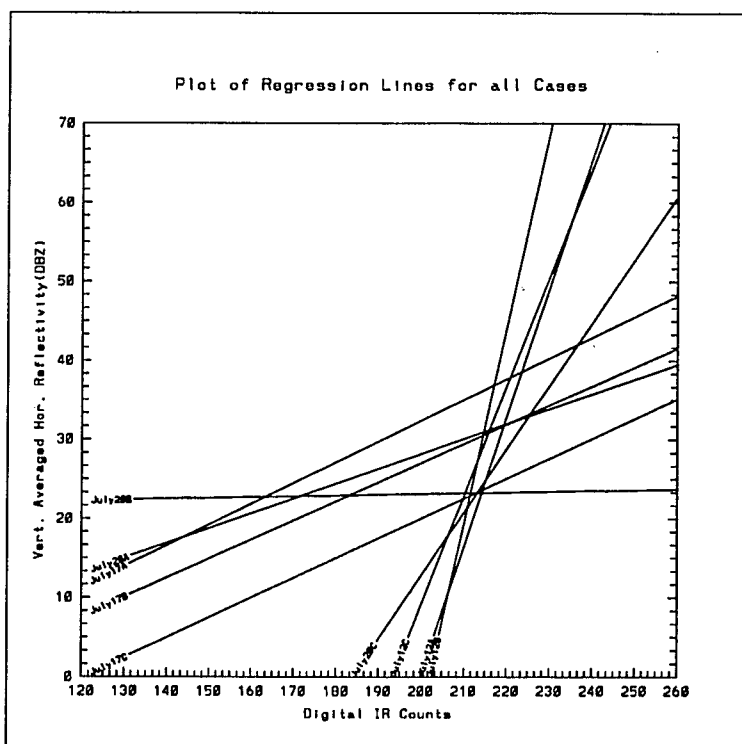


Figure 5. IR-DBZ Regression Lines.

Presentation of all regression lines produced in this analysis. Each line is labeled with the corresponding sample identifier listed in Table 1.

lines 17a and 17b, and lines 20a and 20b, were compared for the storms studied on July 17th and July 20th, respectively. In every case, the null hypothesis that the two regression variances were estimates of a common variance was accepted.

As a result, the slopes of each pair were compared. In this case, however, significant differences were found between the slopes of 12b and 12c, and those for 20a and 20b. Only the slopes of regression lines 17a and 17b could be considered parallel, and therefore, only these two regression lines were tested for coincidence. Unlike the hypotheses of similar variances and parallel slopes, the null hypothesis of coincident regression lines was rejected. Thus, it was concluded that combination of regression lines representing the same cloud type, convective or stratiform, and lying within the same case study is not statistically possible. This implies that no common linear relationship exists among stratiform or convective cloud regions.

Further verification of the last statement comes from attempts to combine all convective or stratiform regression equations regardless of the storm in which they were observed. As with combination of the two convective or two stratiform regression lines within a case, combination of all convective(12a, 17a, 17b, 20a, and 20c) or stratiform(12b, 12c, 17c, and 20c) equations was not possible. In both instances, differences between variances were found to be significant. Therefore, several other combinations were tried.

Since the regression statistics of July12A resembled the stratiform samples more than the convective samples, it was felt that removing it from the convective group and includ-

ing it with the stratiform group might improve the results of the variance test for both. This was not the case. Similarly, since the stratiform sample, July17C, showed statistical similarities to the convective types, it was included with the convective group. The results were the same, significant differences still existed among the variances.

Only removal of the regression lines with the highest and lowest variances (Table 2) effected the results. Although the variances among the stratiform groups were still incompatible, the variances of the three remaining convective regression lines, 12a, 17a, and, 17b, were now considered similar. Having passed the variance test, the slopes of these lines were then compared with negative results. In light of these first two comparisons, it appears that the specific characteristics of each regression line depends on the storm type, stage of storm development, and day of observation.

Attempts to combine the three regression lines representing a particular case resulted in failure for all storms. In each case, July12th, July17th, and July20th, significant differences were found among the regression variances of each sample and the null hypothesis was rejected. This was not entirely surprising due to the clear differences between the regression variances listed in Table 2, and the nature of the convective and stratiform regression lines of

each storm as illustrated in Figure 5.

Comparison of all nine regression lines produced in the study displayed an even stronger tendency toward dissimilar variances. In considering the results of the previous test this was to be expected. Inability to combine these regression lines, representing both stratiform and convective clouds, denies the existence of any regional linear IR and DBZ relationship.

As a result of this analysis it appears that any relationship found between digital IR counts and vertically averaged horizontal reflectivities is tenuous at best. Although this might be anticipated for the dynamic convective regions, the lack of any consistent relation among the more benign stratiform types is somewhat surprising. Evidently, the different morphology within each system, ranging from an unorganized multicellular cluster to a highly organized meso-alpha scale convective complex, is sufficient to produce considerable variations among the internal structure of these storms. This influences the microphysical properties of the drop size distributions, and ultimately effects radar reflectivity and any relation it may have with digital IR counts, or infrared cloud top temperatures. The lack of any consistent relation between the two has also been noted by Reynolds and Smith(1979). Thus, the linear relationships found between the vertically averaged horizontal radar reflectivity and digital infrared counts of each GOES

image must be considered instantaneous, and therefore, it seems apparent that a universal linear DBZ-IR relationship for convective or stratiform cloud types does not exist for these samples.

6. Results of Daily Rainfall Estimation

The final aspect of this analysis involved the estimation of daily precipitation volumes. This was done through the hourly computation of surface rainfall using $Z = 55R^{1.6}$ and vertically averaged horizontal radar reflectivity fields, which were generated from GOES infrared images using the regression equations presented in Table 3. Once hourly precipitation volumes were compiled for each grid point in the analysis domain, daily rainfall totals were determined using three different estimation techniques.

The first, or grid point method, produced daily rain volume estimates by simply summing the hourly rain volumes at each grid point. The second method, or ATI approach, employed an area-time integral, where the 24 hour rainfall estimate was the product of a slope parameter and the precipitation area within an optimal rainrate threshold. This was illustrated by equation 6. Both the slope parameter, $S(t)$, and the threshold, t , were determined empirically from a linear regression of average areawide rainrates, R , against the fractional coverage, $F(t_1)$, of rainrates above specific rainfall thresholds, t_1 . The final estimation

technique, better known as HART, is essentially the same as the second except that the average areawide rainrate is multiplied by an effective precipitation efficiency before the regression was performed. This had the effect of reducing the average areawide rainrate in accord with the depleting effects of such phenomena as local evaporation.

To estimate surface rainfall with each of the methods discussed above, the surface rainfall distribution corresponding to each hourly GOES image had to first be created. This was accomplished using three different pairings of regression equations to generate the internal reflectivity fields, which were then used to produce hourly rainfall distributions. Thus, the daily rain volume estimation involved the application of the grid point, ATI, and HART methods to the rainfall distributions created from hourly GOES infrared images using three different sets of regression equations.

First of all, rainfall distributions were estimated from hourly GOES infrared images using the regression equations derived on a case by case basis. Therefore, only regression relations for July 12th will be used to estimate surface rainfall on July 12th, where the convective(stratiform) relation will be applied at grid points deemed convective(stratiform) by the convective/stratiform delineation technique. In the case of duplicate regression equations(i.e. two representing the same cloud type), the re-

gression equation providing the highest correlation coefficient will be used. As a result, the case specific equations used in the rainfall estimation on July12th were 12a and 12b, those for July17th were 17a and 17b, while those for July20th were 20a and 20c. These equations are listed in Table 3.

The second volumetric rainfall estimation will be performed using the stratiform and convective regression equation which indicate the strongest linear relationships, or in other words, have the highest correlation coefficients. In this case, equation 17a will be used to estimate internal radar reflectivity at all convective grid points and equation 12b will be used at all stratiform pixels.

Although earlier statistical analysis suggested otherwise, an alternative precipitation estimation will involve two regression equations resulting from combination of the two best convective and stratiform relations, respectively. Since July17A and July17B have the highest correlation coefficients among convective types, equations 17a and 17b were combined to form a regression equation which will be applied at all convective grid points. Similarly, for reflectivity estimation from digital IR counts at stratiform grid points, the regression equation resulting from the combination of equations 12b and 12c will be used.

Before rainfall estimation could begin, effective rainrate thresholds and slope parameters had to be deter-

mined for both the ATI and HART approaches. The regression of average areawide rainrate, R , against the fractional coverage, $F(t_1)$, of precipitation with rainrates greater than or equal to t_1 , across all reflectivity images, yielded an effective precipitation threshold of 6 mm hr^{-1} , and a slope parameter of 14.61 mm hr^{-1} for the ATI approach. Regression analysis for the HART method, involving precipitation efficiencies of Texas, resulted in $t = 6 \text{ mm hr}^{-1}$ and $S(t) = 11.69 \text{ mm hr}^{-1}$. The resulting regression lines, and distribution of R , $F(t_1)$ pairs about the regression line are presented in Figure 6. The most notable feature of the diagrams are the high correlation coefficients and small scatter about the regression lines. The smaller slope of the regression line obtained with the HART method is also evident.

Results of volumetric precipitation estimates for each regression line combination are presented in Table 4, along with actual volumetric rainfall obtained from surface rain-gauges. Actual daily volumetric totals were obtained by first mapping the irregularly spaced daily rain-gauge amounts into a $720 \times 720 \text{ km}^2$ rectangular grid centered on the storms which provided the radar data. This was performed in the same manner as that for the low resolution infrared data. After the mapping, daily rain volumes were simply computed as the sum of rain volumes at each grid point within the analysis domain. Due to the scarcity of the

Mexican rainfall data and the highly variable spatial distribution of surface rainfall, the remapping of the irregular gauge data into a regular grid will introduce some uncertainty into the actual rain volumes computed. However, this was felt necessary in order to obtain reasonable estimates of daily rain volumes.

Having reviewed the method of rainfall estimation, discussion of the results will proceed in two ways. First of all, rain volumes estimates will be looked at in terms of the pairing of regression equations utilized to estimate the internal radar reflectivity, and thus the rainfall distribution, from the infrared GOES images. Secondly, the results will be considered from the viewpoints of the three rainfall estimation techniques employed, namely, the grid point, ATI and HART methods.

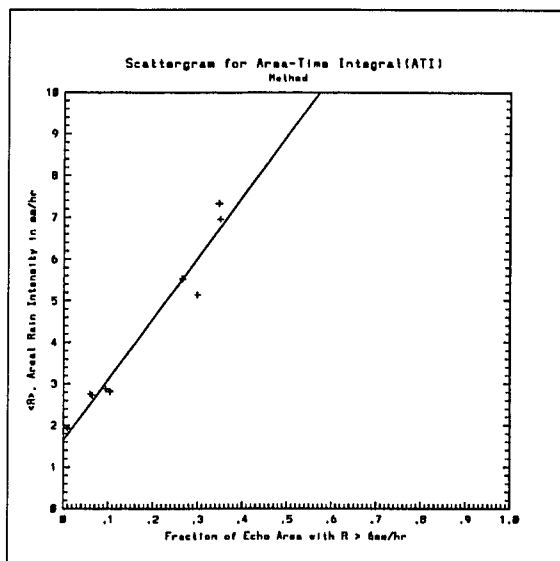
Consideration of the precipitation estimates in terms of the regression equations used, indicates that use of the case specific regression lines produced the overall best estimates of surface rain volumes. With this scheme, over estimation was almost as likely to occur as underestimation, while the other regression equation pairings predominantly overestimated the actual. In fact, all precipitation estimates involving the best convective(17a) and best stratiform(12b) regression equations were larger than those observed.

Application of equations 17a and 12b to the satellite

images of July 12th produced daily volumetric totals up to eight times the observed value of 2.42×10^{18} mm³. Although the use of these regression equations with the July 17th and July 20th infrared images still resulted in overestimates, these numbers were more reasonable, typically a factor of one or two above the actual daily totals of 2.91×10^{18} mm³ and 6.11×10^{18} mm³, respectively. Similar results were obtained using the convective and stratiform regression equations resulting from combining the two best convective and stratiform regression lines, respectively.

Qualitatively, the better performance of the case specific regression equations can be seen in the average ratio of estimated to actual precipitation and the standard deviation of this ratio. Since each regression equation grouping produced nine rainfall estimates, as indicated in Table 4, these numbers are computed from the ratios obtained by comparing each of the nine rainfall estimates with the actual daily rain volume computed for each sample. For the case specific regression lines, the average ratio of estimated rain volumes to the observed rain volumes was 1.12 with a standard deviation of 0.64. These numbers are much lower than the average ratios (3.59, 2.85) and standard deviations (2.91, 2.45) calculated from the volumetric totals obtained using equations 17a and 12b, and those resulting from combination of the two best convective and two best stratiform equations. This was to be expected in light

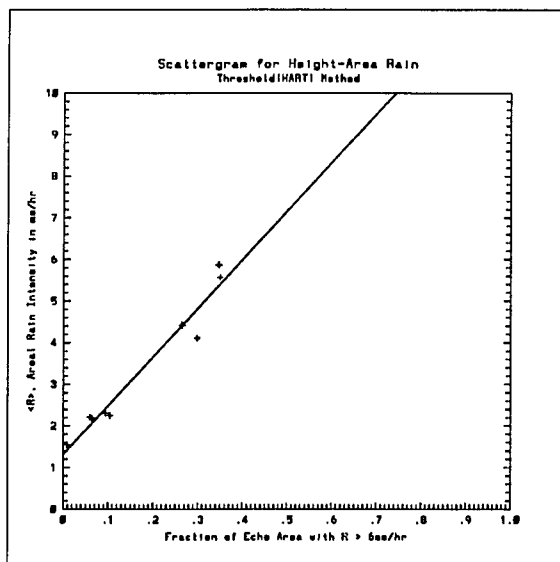
Figure 6. Scatter Diagrams for ATI/HART Slope Parameter Estimation



$$t = 6 \text{ mm hr}^{-1}$$

$$\text{Corr. Coef.} = .97$$

$$\text{Std. Dev.} = .45$$



$$t = 6 \text{ mm hr}^{-1}$$

$$\text{Corr. Coef.} = .98$$

$$\text{Std. Dev.} = .36$$

Figure 6 - Scatter diagrams for ATI and HART slope parameter estimation.

Scatter diagrams used in the estimation of the slope parameters for both the ATI and HART rainfall estimation techniques. Correlation coefficients, standard deviation, and optimal rainrate threshold for $F(t)$ and R pairs in each analysis are included in test blocks to the right of the corresponding diagram.

Table 4. Rainfall Estimation Results

a. Best Convective and Stratiform Regression Equations for each case.

| | <u>ATI Method</u> | | <u>HART Method</u> | | <u>Grid Point Method</u> | |
|---------------|---------------------|-------------------------------|---------------------|-------------------------------|--------------------------|-------------------------------|
| | <u>slope(mm/hr)</u> | <u>volume(mm³)</u> | <u>slope(mm/hr)</u> | <u>volume(mm³)</u> | <u>Slope(mm/hr)</u> | <u>volume(mm³)</u> |
| July 12, 1990 | 14.61 | 1.59x10 ¹⁸ | 11.69 | 1.27x10 ¹⁸ | 29.00 | 3.17x10 ¹⁸ |
| July 17, 1990 | 14.61 | 6.26x10 ¹⁸ | 11.69 | 5.01x10 ¹⁸ | 12.44 | 5.33x10 ¹⁸ |
| July 20, 1990 | 14.61 | 3.76x10 ¹⁸ | 11.69 | 3.00x10 ¹⁸ | 17.79 | 4.57x10 ¹⁸ |

b. Best Overall Convective and Stratiform Regression Equations

| | <u>ATI Method</u> | | <u>HART Method</u> | | <u>Grid Point Method</u> | |
|---------------|---------------------|-------------------------------|---------------------|-------------------------------|--------------------------|-------------------------------|
| | <u>slope(mm/hr)</u> | <u>volume(mm³)</u> | <u>slope(mm/hr)</u> | <u>volume(mm³)</u> | <u>slope(mm/hr)</u> | <u>volume(mm³)</u> |
| July 12, 1990 | 14.61 | 1.99x10 ¹⁹ | 11.69 | 1.59x10 ¹⁹ | 13.25 | 1.81x10 ¹⁹ |
| July 17, 1990 | 14.61 | 6.26x10 ¹⁸ | 11.69 | 5.01x10 ¹⁸ | 12.43 | 5.32x10 ¹⁸ |
| July 20, 1990 | 14.61 | 1.01x10 ¹⁹ | 11.69 | 8.08x10 ¹⁸ | 12.30 | 8.49x10 ¹⁸ |

c. Combination of Two Best Convective and Two Best Stratiform Regression Lines

| | <u>ATI Method</u> | | <u>HART Method</u> | | <u>Grid Point Method</u> | |
|---------------|---------------------|-------------------------------|---------------------|-------------------------------|--------------------------|-------------------------------|
| | <u>slope(mm/hr)</u> | <u>volume(mm³)</u> | <u>slope(mm/hr)</u> | <u>volume(mm³)</u> | <u>slope(mm/hr)</u> | <u>volume(mm³)</u> |
| July 12, 1990 | 14.61 | 1.77x10 ¹⁹ | 11.69 | 1.42x10 ¹⁹ | 9.48 | 1.15x10 ¹⁹ |
| July 17, 1990 | 14.61 | 5.23x10 ¹⁸ | 11.69 | 4.19x10 ¹⁸ | 9.38 | 3.36x10 ¹⁸ |
| July 20, 1990 | 14.61 | 7.98x10 ¹⁸ | 11.69 | 6.38x10 ¹⁸ | 10.46 | 5.71x10 ¹⁸ |

d. Actual Rainfall Volumes(mm³)

| | |
|---------------|-----------------------|
| July 12, 1990 | 2.42x10 ¹⁸ |
| July 17, 1990 | 2.91x10 ¹⁸ |
| July 20, 1990 | 6.11x10 ¹⁸ |

Table 4. Rainfall Estimation Results.

Summary of daily rain volume estimation for each case study using ATI, HART, and grid point summations.

of the regression and correlation analysis. Since the linear relationships found between the vertically averaged horizontal reflectivities and digital infrared counts were seen to vary with storm type and stage of development, it seems reasonable that the case specific regression equation application out performed the applications of regression equations to climatologies other than those in which the relationships were derived.

In assessing the effectiveness of the grid point, ATI, and HART prediction schemes, analysis of the ratio of the estimated rain volumes to the actual rain volumes, and the standard deviation of this ratio, were considered. In this case, the average ratio and standard deviations of each approach, were determined by comparing all such ratios within each of the three methods. While the HART method showed the lowest average ratio (2.30) and median standard deviation(2.27) among the predictions, the simple summation of rain volumes on a grid point basis displayed the lowest standard deviation(2.25) and the median average ratio(2.38). The ATI method, on the other hand, produced the largest average ratio(2.98) and standard deviation(2.83) of all rainfall estimates. Thus, in this analysis, HART gave the closest predictions, while the grid point method seems more consistent in its prediction error.

Comparison of the HART and the ATI approaches, indicates estimates which are different only by a factor equal to the

ratio of their respective slope parameters (~1.25), with the ATI method producing higher estimates in every case. This is no surprise since the two methods differ only by this constant, which is higher for the ATI approach. In this analysis, the HART method produced much better rain volume estimates than the ATI method. Since both methods are area-time integral approaches, the better estimates by HART were a direct result of including precipitation efficiencies. These had the effect of reducing the slope parameter for HART, and therefore, the precipitation estimates resulting from multiplication of the slope parameter with the area covered by rainrates greater than or equal to 6 mm hr^{-1} .

The overall performances of the grid point and HART methods, on the other hand, were so similar that it is hard to say which one was better. Although the average ratio between the grid point and HART estimates was only 0.20, while the standard deviation among these ratios was 0.53, the HART volumetric totals were closer to the actual five out of nine times. This may suggest that HART provided better estimates. But in reality, due to the uncertainty surrounding the Mexican rainfall data and therefore, the actual daily rainfall volumes, it would be erroneous to make a conclusion one way or the other.

Additional uncertainty arises through consideration of the slope parameters used in the area-time integral approaches. In general, the HART and ATI methods have been

found to be effective schemes for estimating precipitation from either ground based or space borne radars, provided that one obtains a representative radar sample of convective cells in varying stages of development. The most efficient means for acquiring such a sample is to take a snapshot of a domain large enough ($>10^4$ km²) to contain numerous storms in different phases of their lifecycles, or alternatively, to take many samples of one convective storm over its entire lifetime. If this condition is met the slope parameter, $S(t)$, obtained from the precipitation probability density function(pdf) using equation 8, is approximately equal to the slope parameter obtained through a linear regression of average areawide rainrates against the fractional coverage of rainrates above specific thresholds (Rosenfeld, Atlas, and Short, 1990; Atlas, Rosenfeld, and Short, 1990).

In this experiment neither of these two conditions were met, as the pdf was derived from three random radar snapshots within three different convective storms. In this case, $S(t)$ obtained through the regression of areawide rainrates against fractional coverages without consideration of precipitation efficiencies was 14.61 mm hr⁻¹, while $S(t)$ obtained using equation (8) was 25.51 mm hr⁻¹. This difference in the slope parameters suggests that the radar samples utilized to derive the rainfall probability distribution were insufficient to provide a representative number

of cells.

The relative inaccuracy of $S(t)$ obtained from the pdf is further indicated by the effective slope parameters computed from the grid point approach and listed in column 5 of Table 4. All but one of these parameters tend toward the lower slope parameter obtained from the regression analysis of average areawide rainrates and fractional coverages. Therefore, in consideration of the uncertainty discussed above, the relative accuracies of each of the three precipitation estimation schemes utilized in this analysis remains a point of conjecture.

7. Summary and Conclusions

The preceding analysis implemented and evaluated a new satellite rainfall estimation technique. First it was determined whether and how satellite infrared cloud top temperatures (digital IR counts) were related to vertically averaged internal radar reflectivities. Relations were sought using correlation and least squares linear regression analysis on nine internal radar reflectivity samples and corresponding hourly GOES infrared images. These reflectivity samples were obtained during airborne doppler analysis of three significantly different mesoscale convective systems, with morphologies ranging from an unorganized multicellular cluster to a highly organized meso-alpha scale convective complex. Of these nine samples, five

were deemed convective and four stratiform by in-flight observers during SWAMP, based on radar characteristics and visual verification.

After positive linear relationships were found, the resulting regression equations were compared to determine if any relations between convective and stratiform samples of one case could be considered equal to those of another case. In other words, the possibility of a climatological, convective or stratiform linear DBZ-IR relation was examined, not to mention the possibility of combining stratiform and convective regression lines into one universal relation, which would be applicable to more than one cloud type.

Finally, the linear relations derived in phase one were used to estimate daily surface rainfall. To this end, three convective/stratiform regression equation pairings were employed: 1) the best (i.e. highest correlation coefficient) convective and stratiform equation of each storm; 2) the best convective and stratiform equations among all cases; and 3) the two regression equations resulting from combining the two best convective and two best stratiform equations. With these regression equation pairs, internal radar reflectivities were estimated from hourly GOES infrared images and used in conjunction with $Z = 55R^{1.6}$ to generate hourly surface rainfall amounts for each grid point. From these grid point values, volumetric rainfall amounts were

computed using a straight area-time integral(ATI) approach, the Height-Area Rainfall Threshold(HART) method, and by simply summing up the grid point values.

The regression analysis of part one showed that a significant positive relationship between digital IR counts and vertically averaged internal radar reflectivities existed for most stratiform samples and for convective samples of MCS's in the early stages of their lifecycle. Thus, since highest digital counts correspond to the coldest cloud top temperatures, it was inferred that cold cloud tops were associated with high internal reflectivities in stratiform and developing convective samples, while mature convective regions displayed insignificant positive correlations. The greater consistency shown among stratiform types was felt to result from the greater homogeneity of both the IR and DBZ fields associated with these clouds. The convective regions, on the other hand, had fewer significant correlations due to the highly cellular and dynamical nature of these regions, which produced considerable variability in both the IR and DBZ grids, not to mention the obscuring effects of anvil development.

Finding positive correlations in part one of this experiment lead to the investigation of the nature of these relationships. Were these relations dictated by the system type and climatology of the day? Or did universal relationships exist among stratiform, convective or all types? To

answer these questions attempts to statistically combine these regression lines were made according to procedures spelled out in Brownlee(1965). However, all attempts to combine convective(stratiform) lines, both within or across cases, met with failure in all statistical tests. Therefore, it was concluded that any linear relation found between digital IR counts, or cloud top temperatures, and internal radar reflectivities were tenuous, and appeared to vary with the cloud type, stage of system development, and climatology of the day. Thus, it would seem that no universal relationship exists between the digital IR counts and internal radar reflectivities of both convective and stratiform cloud samples used in this analysis.

The final aspect of this study involved estimating daily surface rain volumes from GOES images using three rainfall estimation techniques in tandem with three combinations of regression equations. In general, both the HART and grid point approach out performed the ATI method. However, definitive conclusions could not be drawn due to the uncertainties surrounding the Mexican rainfall data and the suggested misrepresentation of the precipitation probability density function by the nine vertically averaged horizontal reflectivity samples.

In terms of the regression equation pairings, it was inferred that storm specific application of these equations performed much more consistently than the other two combi-

nations, which resulted in precipitation estimates as much as eight times larger than the approximate daily rain volumes. The case specific equations, on the other hand, were typically within a factor of two.

Overall it is felt that this analysis went fairly well with several possible areas for improvement. More radar samples and complete area wide storm coverage would have facilitated both the regression analysis and the estimation of surface rainfall. Full instantaneous storm coverage would have limited the movement of the radar echoes within the satellite infrared image and any uncertainties surrounding the overall placement of the radar images within the corresponding cloud shield. This could have been accomplished using a radar with a 10cm wavelength instead of a 3.5cm wavelength. Extension of areal storm coverage would also have provided a better distribution of areawide rainfall and have therefore, improved the volumetric rainfall estimation using the area-time integral approaches. Rainfall estimates may also have been improved with a denser surface raingauge network or with a ZR relationship derived from precipitation systems along the west coast of the Sierra Madre Occidental.

In terms of the regression results, increasing the number of radar samples, or obtaining samples from different storm systems with similar morphologies, would have allowed better indication of any trends lying within the convective

and stratiform regression results. The fact that compared regression equations originated from different storm systems in varying stages of development may have lead to the lack of a climatological relationship. However, this does not alleviate the possibility of common linear relations between stratiform and convective regions of similar storm systems.

References

- Adang, T. C., and R. L. Gall, 1989: Structure and Dynamics Dynamics of the Arizona Monsoon Boundary. *Mon. Wea. Rev.*, 117, 1423-1438.
- Adler, R. F., and A. J. Negri, 1987: A Satellite Infrared Technique to Estimate Tropical Convective and Stratiform Rainfall. *J. Appl. Meteor.*, 27, 30-51.
- Adler, R. F., and R. A. Mack, 1983: Thunderstorm Cloud Height-Rainfall Rate Relations for use with Satellite Rainfall Estimation Techniques. *J. Clim. Appl. Meteor.*, 23, 280-296.
- Atlas D., 1990: Radar in Meteorology. *Amer. Meteor. Soc.*, Boston, 806pp.
- Atlas D., Rosenfeld, D., and D. A. Short, 1990: The Estimation of Convective Rainfall by Area Integrals. Part 1, The Theoretical and Empirical Basis. *J. Geophys. Res.*, 95, 2153-2160.
- Atlas, D., D. Rosenfield, and D. B. Wolff, 1990: Climatologically Tuned Reflectivity-Rain Rate Relations and Links to Area-Time Integrals. *J. Appl. Meteor.*, 29, 1120-1135.
- Bartels, D. L., D. P. Jorgenson, and B. F. Smull, 1991: Airborne Doppler Analysis of a Mesoscale Convective System Observed During the SW Area Monsoon Project. Preprints, 25th Intl. Conf. on Radar Meteor., *Amer. Meteor. Soc.*, Paris, 486-489.
- Battan, L. J., 1973: Radar Observation of the Atmosphere. *Univ. of Chicago Press*, Chicago, 324pp.
- Bohren, C. F., and D. R. Huffman, 1983: Absorption and Scattering of Light by Small Particles. *John Wiley & Sons*, New York, 530pp.
- Brownlee, K. A., 1965: Statistical Theory and Methodology. *John Wiley & Sons, Inc.*, New York, 590pp.

- Chervin, R. M., and S. H. Schneider, 1975: On Determining the Statistical Significance of Climate Experiments with General Circulation Models., J. Atmos. Sci. 33, 405-412.
- Crutcher, H. L., and J. M. Meserve, 1966: Selected Level Heights, Temperatures and Dew Points for the Northern Hemisphere. Published by the direction of Commander, Naval Weather Service Command, U.S. Government Printing Office, Washington.
- Douglas, M. W., R. A. Maddox, K. W. Howard, and S. Reyes, 1991a: The Mexican Monsoon. Submitted to J. Clim.
- Douglas, M. W., R. A. Maddox, and K. W. Howard, 1991b: The Summer Monsoon Over Northwestern Mexico: Results from the Southwest Area Monsoon Project. Preprints, V. Congresso Nacional de Meteorologia, Cd. Juarez, Chihuahua, Mexico, October 1991.
- Gamache, J. F., and R. A. Houze, Jr., 1982: Mesoscale Air Motions Associated with a Tropical Squall Line. Mon. Wea. Rev., 110, 118-135.
- _____, and _____, 1985: Further Analysis of the Composite Wind and Thermodynamic Structure of the 12 September GATE Squall Line. Mon. Wea. Rev., 113, 1241-1259.
- Howard, K. W., and R. A. Maddox, 1988b: Mexican Mesoscale Convective Systems - A Satellite Perspective. Preprints, III InterAmerican and Mexican Congress of Meteorology, Mexico City, 404-408.
- Leary, C. A., and E. N. Rappaport, 1983: Internal Structure of a Mesoscale Convective Complex. Preprints 21st Conf. Radar Meteorology, Edmonton, Amer. Meteor. Soc., 70-77.
- Leary, C. A., and R. A. Houze, Jr., 1978: The Structure and Evolution of a Tropical Cloud Cluster. J. Atmos. Sci., 36, 437-457.
- Maddox, R. A., 1980: Mesoscale Convective Complexes.

- Bull. Amer. Meteor. Soc., 61, (11), 1347-1387.
- _____, 1983: Large Scale Meteorological Conditions Associated with Midlatitude, Mesoscale Convective Complexes. Mon. Wea. Rev., 111, 1475-1493.
- Maddox, R. A., M. Douglas, and K. W. Howard, 1991: Mesoscale Precipitation Systems Over Southwestern North America: A Warm Season Overview. Preprints, Intl. Conf. on Mesoscale Meteor. and TAMEX, Taiwan.
- Maddox, R. A., and K. W. Howard, 1988a: Mexican Mesoscale Convective systems - Large Scale Environmental Conditions. Preprints, III InterAmerican and Mexican Congress of Meteorology, Mexico City, 404-408.
- _____, and _____, 1988b: Mexican Mesoscale Convective Systems - Two Case Examples. Preprints, III Inter-American and Mexican Congress of Meteorology, Mexico City.
- Maddox, R. A., K. W. Howard, and A. J. Negri, 1992: Wide-Area, Long-Term Satellite Rain Estimation Using GOES High Resolution Imagery. Preprints, 6th Conf. on Satellite Meteor. and Oceanography, Amer. Meteor. Soc., Atlanta.
- _____, _____, and _____, 1992: Analysis of GOES Infrared Convective Cloud-Top Temperatures For Extended Periods: An Overview of the 1990 Warm Season For a Subtropical Region. Preprints, 6th Conf. on Satellite Meteor. and Oceanography, Amer. Meteor. Soc., Atlanta.
- Masters, J. M., and J. A. Leise, 1990: Correction of Inertial Navigation with LORAN-C on NOAA's P-3 Research Aircraft. Aircraft Operations Center/NOAA. Submitted to J. Atmos. and Oceanic Tech., 1990.
- Meitin, J., K. W. Howard, and R. A. Maddox, 1991: SW Area Monsoon Project: Daily Operations Summary. Available from National Severe Storms Laboratory, Norman, Ok, 115pp.

- Miller, I., and J. E. Freund, 1977: Probability and Statistics for Engineers. Prentice-Hall, Inc., New Jersey, 529pp.
- Moore, T. J., R. J. Gall, and T. C. Adang, 1989: Disturbances Along the Arizona Monsoon Boundary. Mon. Wea. Rev., 117, 932-941.
- Reynolds, D. W., and E. A. Smith, 1979: Detailed Analysis of Compositied Digital Radar and Satellite Data. Amer. Meteor. Soc., 60, 1024-1037.
- Rosenfeld, D., D. Atlas, and D. A. Short, 1990: The Estimation of Convective Rainfall by Area Integrals. Part 2, The Height-Area Rainfall Threshold(HART) Method. J. Geophys. Res., 95, 2161-2176.
- Saucier, W. J., 1955: Principles of Meteorological Analysis. Univ. of Chicago Press, Chicago, 438pp.
- Saunders, P. M., and F. C. Ronne, 1962: A Comparison Between Height of Cumulus Clouds and the Height of Radar Echoes Secured From Them. J. Appl. Meteor., 1, 296-302.
- Schlatter, T. W., 1986: The Use of Computers for the Display of Meteorological Information. Mesoscale Meteorology and Forcasting. Amer. Meteor. Soc., 1986.
- Schuur, T. J., 1991: Airborne Doppler Observation of a Mesoscale Convective System Over the Sierra Madre Occidental Mountains of Mexico. Preprints, 25th Intl. Conf. on Radar Meteor., Amer. Meteor. Soc., Paris.
- Smith, B. F., and R. L. Gall, 1989: Tropical Squall Lines of the Arizona Monsoon. Mon. Wea. Rev., 117, 1553-1569.
- Smith, E. A., and D. R. Phillips, 1972: Automated CLOUD Tracking Using Precisely Aligned Digital ATS Pictures. IEEE Trans. on. Comp., C-21, 715-729.

- Smull, B. F., and R. A. Houze, Jr., 1985: A Midlatitude Squall Line with Trailing Region of Stratiform Rain: Radar and Satellite Observations. *Mon. Wea. Rev.*, 113, 117-133.
- _____, and _____, 1987: Dual-Doppler Analysis of a Midlatitude Squall Line with a Trailing Region of Stratiform Rain. *J. Atmos. Sci.*, 44, 2128-2148.
- _____, and _____, 1987: Rear Inflow in Squall Lines with Trailing Stratiform Precipitation. *Mon. Wea. Rev.*, 115, 2869-2889.
- Walpole, R. E., and R. H. Meyers, 1989: *Probability and Statistics for Engineers and Scientists*. Macmillan Publishing Company, New York, 765pp.
- Watson, A. I., J. G. Meitin, and J. B. Cuning, 1988: Evolution of the Kinematic Structure and Precipitation Characteristics of a Mesoscale Convective System on 20 May 1979. *Mon. Wea. Rev.*, 116, 1555-1567.
- Weisman, M. L., and J. B. Klemp, 1986: Characteristics of Isolated Convective Storms. *Mesoscale Meteorology and Forecasting.*, Amer. Meteor. Soc., 1986.
- Zawadski, I., 1984: Factors Affecting the Precision of Radar Measurements of Rain. Preprints, 22nd Conf. Radar Meteorology, Zurich, Amer. Meteor. Soc., 251-256.